ACID JETTING COMPARISON STUDY USING A MODIFIED ACID SYSTEM IN CARBONATE RESERVOIRS

A Thesis

by

JULIAN ALBERTO URIBE CHACON

Submitted to the Office of Graduate and Professional Studies of
Texas A&M University
in partial fulfillment of the requirements for the degree of

MASTER OF SCIENCE

Chair of Committee,	Ding Zhu
Co-Chair of Committee,	A. Daniel Hill
Committee Member,	Victor Ugaz
Head of Department,	Jeff Spath

August 2020

Major Subject: Petroleum Engineering

ABSTRACT

In carbonate reservoirs, wells are typically stimulated by injecting acid into the formation. The injected acid reacts and dissolves the formation minerals, creating high-conductive flow paths, also known as wormholes. HCl is the most commonly used acid system in well stimulation in these types of reservoirs. However, at low injection rates, HCl results in poor wormholing efficiency. These low injection rates are required for formations with low breakdown pressures, and for stimulating long horizontal wells. Another challenge of acidizing horizontal wells is the even acid distribution along extended laterals. A mechanical diversion technique has shown promising results in enhancing flow distribution along extended laterals by using small nozzles that adjust the completion's local pressure drop to the formation properties. This type of completion causes the injected acid to be jetted into the formation. It has been experimentally demonstrated that acid jetting results in a bulb-like dissolution structure, known as cavity, and also, wormholes are propagated from the cavity face into the rock. However, the high reaction rates of HCl and carbonate formations at low injection rates limit the wormholing efficiency of the acidizing treatments, even when the acid is properly distributed along the lateral. This study presents experimental results of a modified acid system with controlled reaction rates under jetting conditions at various injection rates.

Linear core-flood jetting tests were conducted at a temperature of 190 °F, and various interstitial and jetting velocity conditions. The distance from the nozzle and the rock sample was maintained invariably for all the tests. A returning line allows the acid not flowing through the rock to flow back to a waste tank; this permitted the matrix flux

is constant. Indiana limestone cores of 4-in in diameter and 16-in in length were used. The permeability and porosity were measured, and their values ranged between 1-3 mD and 12-18%, respectively. A modified acid system and 15% HCl were evaluated for wormhole efficiency. Additionally, the modified acid system was used to investigate the effect of jetting velocity, nozzle size, and jetting time on the dissolution structures.

The experimental results indicate that compared to 15% HCl, the modified acid improves cavity growth control and enhances wormhole propagation rates. Longer wormholes and smaller cavities were achieved with the modified acid at similar testing conditions as 15% HCl; this effect is more pronounced as interstitial velocity and jetting velocity increase. Overall, the modified acid matched HCl results at low jetting velocity and out-performed HCl as jetting velocity increased.

DEDICATION

I would like to dedicate this work to my family: Carlos Uribe, Martha Chacon, Carlos A. Uribe, Oscar Uribe, Yeri Uribe, Sofia Uribe, and my girlfriend Lina Rodriguez.

All their support and sacrifices enabled me the opportunity to achieve this goal. Thank you for your unconditional love and for believing in me. I love you.

ACKNOWLEDGMENTS

I would like to thank Dr. Zhu and Dr. Hill for given me the opportunity of working in this project and for all their support during my time at Texas A&M.

I would like to thank my friends for their support in and out of the office and laboratory. I would also like to thank the members of the research group and classmates. And last but not least, I would like to thank to John Maldonado for his help and guidance on the laboratory equipment.

CONTRIBUTORS AND FUNDING SOURCES

This project was made possible by the financial support from ExxonMobil Upstream Research Company, and the chemicals provided by Fluid Energy Group.

NOMENCLATURE

A	Cross-sectional area
A_{nozzle}	Cross-sectional area of the nozzle
β	Mass dissolving power of the acid
β_{15}	Mass dissolving power of the acid at 15% concentration
CT	Computer Tomography
DICOM	Digital Imaging and Communications in Medicine
D_{core}	Core diameter
D_{nozzle}	Inner diameter of the nozzle
ρ_{acid}	Acid solution density
$\rho_{mineral}$	Mineral density
ρ_{water}	Liquid water density
HCl	Hydrochloric acid
k	Permeability
L	Length
L_{core}	Core length
L_{wh}	Wormhole length
LEL	Limited Entry Liner
m_{dry}	Dry (unsaturated) mass of the core sample
m_{wet}	Water-saturated mass of the core sample
MW_{acid}	Molecular Weight of the acid

$MW_{mineral}$	Molecular Weight of the mineral
ΔP	Differential pressure
BPR	Back-Pressure Regulator
$P_{upstream}$	Upstream pressure
$\emptyset$	Porosity
PV_{bt}	Pore Volumes to Break Through
$PV_{bt,opt}$	Optimal value of Pore Volumes to Break Through
Q_{pump}	Pump flow rate
Q	Volumetric flow rate
$Q_{effluent}$	Volumetric flow rate exiting the core
t_{jet}	Jetting time
μ	Fluid viscosity
V_{acid}	Volume of acid required to dissolve a specific volume of rock
V_{bulk}	Bulk volume of the rock
V_{pore}	Pore volume
$V_{CaCO_3,bulk}$	Dissolved bulk volume of calcium carbonate
$V_{CaCO_3,dissolved}$	Corrected dissolved volume of calcium carbonate
v_i	Interstitial velocity / Injection rate
$v_{i,opt}$	Optimal value of Interstitial velocity / Injection rate
v_{jet}	Jetting velocity
v_{wh}	Wormhole propagation rate

v_m	Mineral stoichiometric constant
v_a	Acid stoichiometric constant
x	Volumetric dissolving power of the acid
x_{15}	Volumetric dissolving power of the acid at 15% concentration

TABLE OF CONTENTS

Page

ABSTRACT ii

DEDICATION iv

ACKNOWLEDGMENTS v

CONTRIBUTORS AND FUNDING SOURCES vi

NOMENCLATURE vii

TABLE OF CONTENTS x

LIST OF FIGURES xii

LIST OF TABLES xv

1. INTRODUCTION AND LITERATURE REVIEW 1

1.1. Matrix Acidizing Background 1
1.2. Jetting Stimulation Technique and Experimental Background 5
1.3. Research Objectives 9

2. METHODOLOGY 10

2.1. Sample Preparation 10
2.1.1. Porosity Measurement 11
2.1.2. Permeability Measurement 12
2.2. Acid Jetting Experimental Conditions 15
2.2.1. Jetting Velocity 15
2.2.2. Differential Pressure 17
2.3. Acid jetting experiment 18
2.3.1. Experimental Apparatus 18
2.3.2. Experimental procedure 22
2.4. Sample imaging and 3D visualization 28
2.5. Modified Acid System 31

3. RESULTS AND DISCUSSION 34

3.1. Evaluation Metrics for Acid Jetting 35

3.1.1. $PVbt$ Based on Effluent Flow 38
3.1.2. $PVbt$ Based on Dissolved Rock Volume 40
3.1.3. Wormhole Propagation Rate 44
3.2. Acid Jetting Results Using a Modified Acid System 45
3.2.1. Effect of Vary Jetting Time on Dissolution Structures 45
3.2.2. Effect of Nozzle Size on Dissolution Structures 51
3.2.3. Effect of jetting velocity on the dissolution structures 53
3.3. Acid Systems Comparison 58
3.4. Lessons Learned 64
3.4.1. Sample IL1 64
3.4.2. Sample IL7 and Sample IL8 65
3.4.3. Sample IL9 66

4. CONCLUSIONS AND FUTURE WORK RECOMMENDATIONS 68

REFERENCES 70

APPENDIX A STEP-BY-STEP 3D IMAGE PROCESSING 74

APPENDIX B EXPERIMENTAL RESULTS 79

APPENDIX C PORE VOLUMES TO BREAKTHROUGH METHODS 80

APPENDIX D SUMMARY OF DISSOLUTION STRUCTURE IMAGES 82

LIST OF FIGURES

Page

Figure 1. Schematic of typical laboratory results for matrix acidizing in carbonates 3

Figure 2. Example of the dissolution structure generated by acid jetting 7

Figure 3. Water saturation setup. PVC pipe (left) and vacuum pump (right) 13

Figure 4. Permeability measurement apparatus 14

Figure 5. Acid jetting experimental setup for constant interstitial velocity condition 19

Figure 6. Schematic of the acid jetting core holder (Reprinted from Ridner (2018)) 20

Figure 7. Control valve-actuator combo (left) and weight scale and display (right) 22

Figure 8. (a) Core holder parts and (b) Inlet cap components 23

Figure 9. LabVIEW Interface for Acid Jetting Experiments 24

Figure 10. Toshiba Aquilon CT scanner 28

Figure 11. 3D volume rendering of the dissolution structure 29

Figure 12. Horos™ software built-in functions a) Wormhole length measurement. b) Cavity volume calculation 30

Figure 13. Lysine Chemical Structure 32

Figure 14. Flow path comparison between matrix acidizing and acid jetting experiments 37

Figure 15. Matrix acidizing and acid jetting PV_{bt} – Based on effluent flow 40

Figure 16. Matrix acidizing and acid jetting PVbt – Based on dissolve rock volume 44

Figure 17. CT scan images of injected volume comparison tests. Interstitial velocity increasing from left to right 47

Figure 18. Cavity volume and wormhole length as a function of interstitial velocity for high-volume and low-volume experiments 48

Figure 19. Wormhole propagation rate as a function of interstitial velocity for high-volume and low-volume experiments 49

Figure 20. Cavity growth rate and cavity enlargement rate as a function of interstitial velocity for high-volume and low-volume experiments....50

Figure 21. Effect of nozzle size on dissolution structures with interstitial velocity increasing from left to right....52

Figure 22. Wormhole length and cavity volume as a function of interstitial velocity for both nozzle sizes....53

Figure 23. Effect of jetting velocity on dissolution structures with interstitial velocity and jetting velocity increasing from left to right....55

Figure 24. Cavity growth rate and cavity volume as a function of interstitial velocity for all jetting velocity conditions....56

Figure 25. Wormhole propagation rate as a function of interstitial velocity for all jetting velocity conditions using a modified acid system....57

Figure 26. Dissolution structures of experiments at various interstitial velocities, (a) 65 ft/s, (b) 150 ft/s, and (c) 25 ft/s, all at a temperature of 190 °F, using 15% HCl....59

Figure 27. Comparison of wormhole propagation rate as a function of interstitial velocity for all jetting velocity conditions using 15% HCl....61

Figure 28. Comparison of cavity volume as a function of jetting velocity and interstitial velocity for the modified acid and HCl....62

Figure 29. Comparison of cavity growth rate as a function of jetting velocity and interstitial velocity for the modified acid and HCl....63

Figure 30. Samples IL7 and IL8 - Side rupture....66

Figure 31. (a) Temperature profile of unsuccessful test. (b) Temperature profile of a typical successful test....67

Figure 32. Dissolution structures of the baseline data set (Appendix D)....82

Figure 33. Dissolution structures of the increased v_{jet} data set (Appendix D)....82

Figure 34. Dissolution structures of the decreased vjet data set (Appendix D)....83

Figure 35. Dissolution structures of the decreased nozzle size data set (Appendix D)....83

Figure 36. Dissolution structures of the increased t_{jet} data set (Appendix D)....84

Figure 37. Dissolution structures of the HCl baseline data set (Appendix D) 84

Figure 38. Dissolution structures of the HCl decreased v_{jet} data set (Appendix D)..... 85

Figure 39. Dissolution structures of the HCl increased vjet data set, adapted from Ridner et al. (2020) (Appendix D)..... 85

LIST OF TABLES

Page

Table 1. Summary of all tested samples 11

Table 2. Summary of experimental conditions for all data sets 35

Table 3. Matrix acidizing experiments 38

Table 4. Experimental conditions for jetting time investigation 46

Table 5. Experimental conditions for nozzle size investigation 51

Table 6. Experimental conditions for jetting velocity investigation 54

Table 7. Experimental conditions for acid systems comparison 58

Table 8. Experimental results of all samples (Appendix B) 79

1. INTRODUCTION AND LITERATURE REVIEW

Over half of the world's conventional hydrocarbon reserves are found in carbonate reservoirs (Akbar et al. 2000; Burchette, 2012). Carbonate reservoirs are composed primarily of calcite and dolomite. Hydrocarbon wells in carbonate formations are generally stimulated to enhance well performance by injecting acid into the rock. The most common acid stimulation techniques are matrix acidizing and acid fracturing. This study investigates the matrix dissolution efficiency of a modified acid system under acid jetting applications; acid fracturing is not part of the scope of this project.

1.1. Matrix Acidizing Background

Matrix acidizing is a well stimulation technique in which acid is injected into the formation, causing minerals dissolution, and hence recover or increase the near-wellbore permeability; in carbonate formations, the most commonly used stimulation fluid is hydrochloric acid (HCl) (Economides et al. 2013). The acid solutions are injected at low enough rates that the bottom-hole pressure is maintained below the formation breakdown pressure (Zhu, D. and Furui, K. 2018). Thus, carbonate formations are not fractured during matrix acidizing.

In carbonate formations, the injected acid reacts with the minerals present in the rock, creating artificial, high-conductive flow channels, usually referred to as wormholes (Fredd and Fogler, 1999). Wormholes can extend as much as 10 to 20 ft into the formation; its dissolution structures and patterns are highly dependent on several factors such as injection rate, flow geometry, reaction kinetics, and mass transfer (Furui et al. 2010).

Wang et al. (1993) found the existence of an optimal injection rate for matrix acidizing in carbonate reservoirs. Fredd et al. (1997), and Fredd and Fogler (1999) reported that at high injection rates, the wormhole structures tend to be more extended and branched; and at low injection rates, face dissolution of the rock dominated, and acid was unable to penetrate the carbonate rock. Additional experimental and theoretical studies on matrix acidizing lead to defining an optimal condition for acid injection (Hoefner and Frogler 1989, Paccaloni and Tambini, 1993; Buisje and Glasbergen, 2005; McDuff, 2010; Furui et al. 2010). The optimal injection condition yields the highest efficiency of the acid treatment, creating the longest wormholes into the formation with the less volume of acid injected.

The optimal condition is described by two parameters, the optimal pore volumes to breakthrough ($PV_{bt,opt}$) and the optimal injection rate ($v_{i,opt}$); The pore volumes to breakthrough (PV_{bt}) measures acidizing efficiency, and it is defined as the pore volumes of acid needed for wormholes to break through a given volume of rock (Zhu and Furui, 2018), as presented in Equation 1. Thus, the smaller this parameter is, the less acid is required to propagate wormholes through a given volume of rock, and therefore, the highest efficiency is reached.

$$PV_{bt} = \frac{volume\ of\ acid\ injected}{pore\ volume\ of\ the\ rock} \tag{1}$$

The optimal injection rate is the rate at which the highest efficiency for matrix acidizing treatments is achieved. This condition refers to the lowest PV_{bt}, and it is known as optimal pore volumes to breakthrough ($PV_{bt,opt}$). The optimal injection rate can be

expressed in terms of interstitial velocity, which is defined as the volumetric injection rate divided by the porous cross-sectional area of the rock, i.e., porosity times cross-sectional area. Figure 1 presents the typical efficiency plot for laboratory experiments on carbonate acidizing, where the optimal condition is circled in red. Several researchers have reported that for injection rates below the optimal condition, the efficiency decreases drastically (higher PV_{bt}) as the injection rate decreases; however, for injection rates above the optimal condition, the efficiency increase (lower PV_{bt}) as the injection rate decreases (Wang et al. 1993, Bazil, 2001; Buijse and Glasenbergen, 2005; McDuff et al. 2010; Dong, 2010). Figure 1 shows that if the optimal injection rate is not reached, it is better to have injection rates above the optimal since, for lower rates, the efficiency is lost much faster.

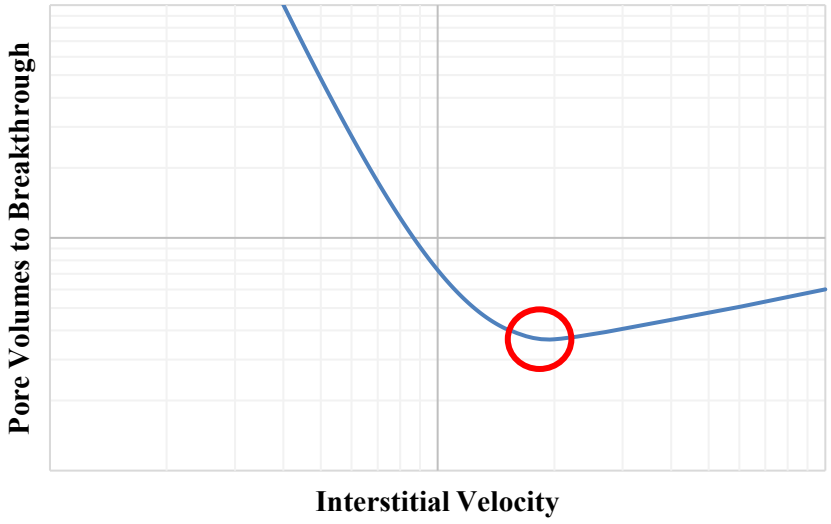

Figure 1. Schematic of typical laboratory results for matrix acidizing in carbonates

Williams et al. (1979) recommended performing carbonate-acidizing treatments at the highest possible injection rate that allows the bottom-hole pressure to stay below the fracturing pressure. However, formation with low breakdown pressures require low

injection rates to prevent fracturing. At these low injection rates, the rapid reaction rate of HCl and calcium carbonate (CaCO3) results in face dissolution and severely limits the acid penetration distance; this face dissolution consumes large volumes of acid and stimulates short distances (Fredd and Fogler, 1997). Low injection rates also result in prolonged contact of the tubulars with HCl, raising corrosion concerns, especially in high-temperature applications. The face dissolution due to low injection rates leads to poor efficiency of the stimulation treatments (Van Domelen and Jennings, 1995). Therefore, alternative acid systems to HCl with improved wormholing efficiency at low injection rates and high-temperature applications are always in demand.

Typical carbonate acidizing treatments in vertical wells are performed by injecting acid into the wellbore through production tubing, coiled tubing, or drill pipe (Mishra et al. 2007). In horizontal wells, acid treatment designs are different. The principal difference resides in the stimulated length of the well. In vertical wells, the stimulated length ranges from tens to hundreds of feet, while in horizontal wells, it can be thousands of feet. Carbonate reservoirs are characterized by their extreme heterogeneity (Lucia et al. 2003; Burchette, 2012). Thus, permeability variations are likely to be encountered, especially in horizontal wells with large contact areas with the formation, i.e., long laterals. The presence of significant permeability variations results in challenges for acid placement and adequate interval coverage during acid stimulation treatments, as more acid volume tends to flow through high-permeability zones, leaving low-permeability zones almost untreated (Pereira et al. 2012). Numerous mechanical and chemical diversion techniques are used to overcome acid placement issues (Pereira et al. 2012; Rahim et al. 2013; Zhu and Furui,

2018). However, carbonate acidizing in wells with long laterals is still under development. Over the years, several field studies have been performed to evaluate the completion techniques that best fit the injection and production requirements for horizontal wells in carbonate reservoirs. These studies include the use of pre-perforated liners, inflow control devices (ICD), chemical diverters, limited entry liners, and ball drop diversion (Jorden et al. 2010, Pereira et al. 2012, Rahim et al. 2013, Issa et al. 2014, Fowler et al. 2014, Hosani et al. 2016, Othman et al. 2018). Results from these studies have demonstrated promising improvements in acid placement and enhanced zone coverage along extended laterals.

From the completion solutions used in pilot wells, limited entry liners combined with isolation packers have shown technical and operational advantages, such as improved flow distribution along the lateral, extended stimulation reach compared to coiled tubing operations, significant post-treatment production increase and operational cost reductions (Rahim et al. 2013, Sau et al. 2014, Hosani et al. 2016, Othman et al. 2018). This study focuses on the dissolution patterns created by an acid jet, based on the concept of limited entry liners for carbonate reservoirs. Linear core-flood experiments are performed to simulate the interaction of a high-velocity acid stream and Indiana limestone rock samples.

1.2. Jetting Stimulation Technique and Experimental Background

Acid jetting has previously been used in the field (Dahroug et al. 2001, Abbasy et al. 2010). These acid jetting jobs were performed injecting acid through coiled tubing, drill pipe, or control acid jet tools, to remove filter cake or near-wellbore damage caused by

drilling fluids invasion. The jetting effectiveness was found to depend on stand-off distance, fluid velocity, jet stream profile, and rotation of the tool (Aslam et al. 2000).

Current acid jetting field applications are conceptually different from previous implementations. Limited entry liners in horizontal wells have shown promising results such as enhanced flow distribution control, operational cost reduction (no coiled tubing), and stimulation of all lateral length (Rahim et al. 2013, Sau et al. 2014, Hosani et al. 2016, Othman et al. 2018). Evenly distributed flow is advantage of this type of completion. The flow distribution control achieved by the limited entry liners is obtained by adjusting the liner's local pressure drop to the reservoir properties and the position of the stimulation zone along the lateral (Beckham et al. 2015). Sau et al. (2014) presented a technique to generate the desire local pressure drop across the limited entry liner by placing small nozzles along the length of the completion. The length of the lateral is compartmentalized through external packers; in each compartment, the nozzle size and density can be modified to the local pressure drop requirements. Conceptually, fewer and smaller diameter nozzles near the heel and increasing density towards the toe are recommended to enhance acid placement. In this stimulation technique, the limited entry liner itself acts as a mechanical diversion system that evenly distributes the acid along the lateral, and thus, enhances the efficiency of the acid treatment.

Similarly to matrix acidizing, acid jetting is a stimulation technique in which acid is injected into the formation at a rate that allows bottom-hole pressure to be maintained below the fracturing pressure of the rock. In addition, acid jetting relies on the mechanical action of the high-velocity acid stream, and the chemical reaction between the acid and

the carbonate rock to stimulate the reservoir (Holland, 2014). Under laboratory conditions, the high-velocity acid stream (acid jet) contacting the rock face creates a bulb-shaped cavity, and wormholes propagate from the cavity into the rock due to acid flux through the sample. Figure 2 shows a typical matrix dissolution structure created by acid jetting, where the acid was jetted from the top, and wormholes propagated from the cavity into the sample. The laboratory jetting technique differs from previous implementations in the field; it was designed accordingly to the current field applications, simulating the concept behind limited entry liner completions.

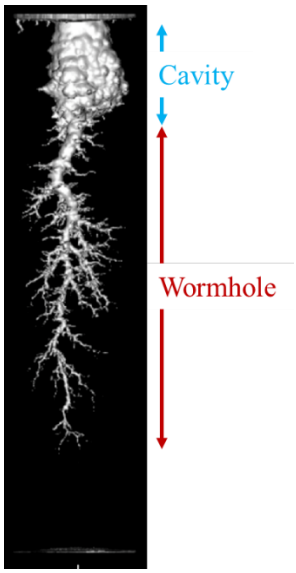

Figure 2. Example of the dissolution structure generated by acid jetting

Initial acid jetting experimental and theoretical studies (Holland, 2014; Ndonhong, 2014; Beckham et al. 2015; Belostrino, 2016) presented insightful information regarding the impact of acid jetting on matrix acidizing using HCl and provided some of the modeling bases for acid jetting. In these studies, a cavity formation was identified as a result of the acid jet impacting the rock face; by using a multi-stage acid jetting procedure,

it was also determined that wormhole and cavity grow concurrently. Moreover, cavity growth and wormhole propagation were found to be controlled by jetting velocity and interstitial velocity, respectively. In addition, as in matrix acidizing, it was concluded that elevated temperatures increased the dissolution rate, and high-permeability samples required more time for the acid to break through the core. However, these acid jetting studies were limited by the experimental apparatus as it was not able to maintain constant interstitial velocity for the whole length of the tests.

More recently, Ridner (2018) and Frick (2018) developed the acid jetting experimental apparatus for constant interstitial velocity tests by adding a remotely controlled needle valve to the effluent line; the valve was manually or automatically operated. This modification allowed the researchers to better understand the impact of acid jetting transport variables on the acid dissolution pattern. HCl was used as the stimulation fluid at two different weight by weight concentrations, 15%, and 28%. It was identified that acid jetting increases wormhole propagation rates compare to matrix acidizing; however, more acid is required in jetting applications. Additionally, cavity growth was found to depend on jetting velocity and to have an exponentially decaying relationship with time. The increase of acid concentration was identified to have a weak but positive effect on the wormhole growth rate, and elevated temperatures increased compact dissolutions, at the point that only cavities were observed in high-temperature tests. Frick (2018) also presented a methodology to evaluate the overall skin factor reduction and dimensionless productivity increase for specific jetting stimulation designs, finding a strong dependence of acid jetting impact on reservoir properties and completion design.

1.3. Research Objectives

Field applications have shown the benefits of acid jetting on flow distribution control and acid placement in horizontal wells with extended laterals, promoting experimental and theoretical studies of the acid jet impact on matrix dissolution. As previously mentioned, these studies have provided valuable information regarding wormhole and cavity growth competition, as well as the effect of parameters such as interstitial velocity, jetting velocity, rock type (permeability), and temperature. However, all of the studies were performed using HCl, which, as previously discussed, has poor stimulation efficiency (face dissolution) at low injection rates and high-temperature applications. Thus, the study of an alternative acid system that enhances wormholing efficiency at low rates, high temperatures, and under jetting applications is required.

This study evaluates a modified acid systems for wormholing efficiency in acid jetting applications at high-temperature conditions for a variety of injection rates. The dissolution structures created from jetting conventional 15% HCl are compared with results from using a modified acid system at similar experimental conditions. Moreover, a parametric study using only the modified acid system investigates the effect of nozzle size variation, jetting time, interstitial velocity, and jetting velocity on the dissolution structures generated by acid jetting.

2. METHODOLOGY

In this section, the methodology used in this study will be presented. The methodology is divided into five separate segments. (1) presents sample preparation, which includes porosity and permeability measurements. (2) shows the acid jetting experimental conditions in terms of practical laboratory parameters such as pump rate and differential pressure. (3) shows the procedure and apparatus used in the acid jetting experiments at a constant interstitial velocity. (4) presents sample imaging and processing, and (5) describes the modified acid system used in this study.

2.1. Sample Preparation

The core samples used in this study were 4-inch diameter by 16-inch length, 12 – 18% porosity, 1.4 – 3.3 mD Indiana Limestone. This rock type is a Mississippian-age grainstone with a relatively homogeneous structure. Indiana Limestone was selected, considering that it is almost entirely calcium carbonate. The average mineralogy values are 97% calcium carbonate (CaCO3), and 3% of other minerals such as magnesium carbonate (MgCO3), aluminum oxide (Al2O3), and silica (SO2) (Hill J. 2020).

This section includes porosity and permeability measurements as part of sample preparation. The diameter and length of the core were also measured individually for all samples. Table 1 presents a summary of all the samples tested in this study, with their corresponding porosity and permeability. The procedure to obtain these parameters is presented further in this section.

Table 1. Summary of all tested samples

Experiment ID	Porosity (%)	Permeability (mD)
IL1	17.2%	2.6
IL2	17.4%	2.7
IL3	13.1%	2.5
IL4	12.5%	2.7
IL5	17.3%	2.3
IL6	16.6%	3.3
IL7	17.1%	2.2
IL8	17.2%	2.7
IL9	17.5%	2.2
IL10	17.5%	2.0
IL11	17.2%	2.3
IL12	17.2%	2.1
IL13	17.5%	2.0
IL14	17.6%	2.0
IL15	17.1%	1.9
IL16	17.0%	2.2
IL17	17.1%	2.1
IL18	17.0%	2.1
IL19	17.0%	2.4
IL20	17.1%	2.0
IL21	16.3%	2.2
IL22	16.4%	2.0
IL23	17.3%	2.0
IL24	17.0%	2.2
IL25	17.2%	2.3

2.1.1. Porosity Measurement

The porosity calculation of the sample requires the dry and wet masses of the core. The dry weight corresponds to the core weight with no water or saturating fluid in it. The dry weight was measured after placing the sample inside an oven for 24 hours at 230°F (110°C). The wet weight corresponds to the weight of the sample fully saturated with water; it was measured immediately following the sample permeability measurement, this

considering that the permeability measurement is performed at steady-state conditions, which require fully-saturation of the interconnected pores of the core.

The porosity is defined as the pore volume per bulk volume of the rock, where the bulk volume was calculated by using the volume equation of a cylinder, and the pore volume was estimated by dividing the mass difference between the wet and dry measurements in the saturating fluid's density. The porosity equation is presented below.

$$\emptyset = \frac{V_{pore}}{V_{bulk}} = \frac{\frac{m_{wet} - m_{dry}}{\rho_{water}}}{\frac{\pi D_{core}^2 L_{core}}{4}} \quad (2)$$

Where $\emptyset$ is porosity, V_{pore} is pore volume, V_{bulk} is bulk volume, m_{wet} is the core's saturated mass, m_{dry} is the core's dry mass, ρ_{water} is the density water (saturating fluid), D_{core} is the core diameter, and L_{core} is the core length. Porosity is a dimensionless parameter, which requires consistent units for all variables.

2.1.2. Permeability Measurement

After measuring the dry mass of the core, the sample was placed in a PVC pipe tube, which was subsequently filled with tap water. The tube was sealed using vacuum grease and then connected to a vacuum pump, as shown in Figure 3. The vacuum pressure used for saturation was 70 kPa. The vacuum effect promotes saturation by extracting the air from the porous media. The saturation process was performed for each sample for a minimum of 8 hours.

Figure 3. Water saturation setup. PVC pipe (left) and vacuum pump (right)

A schematic of the permeability apparatus is shown in Figure 4, which includes a 4-inch core holder, two accumulators, two high-pressure syringe pumps, a hydraulic hand pump, a back-pressure regulator, and a pressure transducer, which ultimately connects to the data acquisition hardware. Once the core was placed inside the core holder, and all the connections were properly fastened, the confining pressure was raised to 500 psi. The syringe pumps were set to a constant water flow rate, which for this study was 15 mL/min for all the tests. The syringe pumps inject oil from the oil reservoir to a piston inside the brine accumulator. The piston prevents the brine from being contaminated with the injected oil. The piston ultimately displaces the brine out of the brine accumulator to the core holder, at a constant rate equal to the oil injection rate.

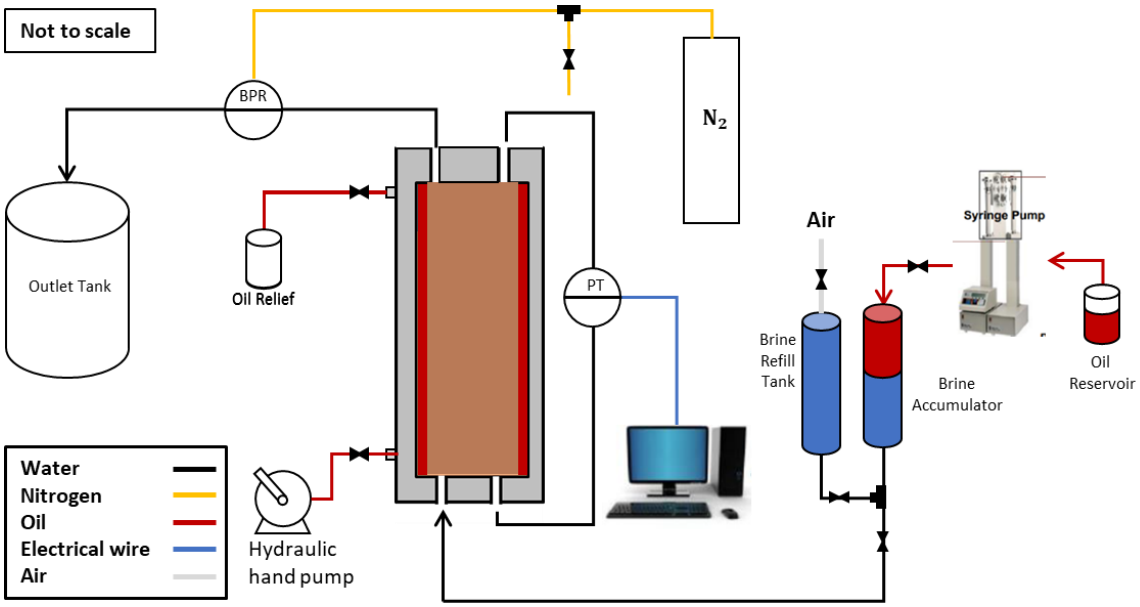

Figure 4. Permeability measurement apparatus

After assuring flow through the core (visible water stream from the outlet line to the outlet tank), the back-pressure regulator was increased to 500 psi. Note that the confining pressure must always be 500 psi greater than the system's pressure to ensure that the water flows through the core and not around it. The water was pumped at a constant rate until pseudo-steady state was reached, i.e., constant differential pressure across the core. Then, the permeability was estimated by using the linear Darcy flow model presented in Equation 3. Refer to Holland (2014) for details on the assembling process for the permeability apparatus.

$$k = 96.13 \frac{QL\mu}{\Delta PA} \tag{3}$$

Where k is permeability in mD, Q is flow rate in mL/min, L is core length in in, μ is viscosity in cp, ΔP is differential pressure across the core in psi, and A is cross-sectional

area of the core in in^2. The conversion factor 96.13 to obtain permeability in mD was calculated as follows:

$$\frac{1\frac{mL}{min}\left(\frac{min}{60\ s}\right)\left(\frac{1\times10^{-6}m^3}{mL}\right)1in\left(\frac{0.0254\ m}{in}\right)1\ cp\left(\frac{0.001\ Pa-s}{cp}\right)}{1\ psi\ \left(\frac{6894.76\ Pa}{psi}\right)1in^2\left(6.45\times10^{-6}\frac{m^2}{in^2}\right)}\left(1.01\times10^{15}\frac{mD}{m^2}\right)=96.13 \quad (4)$$

2.2. Acid Jetting Experimental Conditions

In this study, the experimental conditions were established depending on the temperature, interstitial velocity, and jetting velocity of the test. This section presents the experimental conditions in terms of the laboratory parameters that are manipulated to obtain the desire testing conditions, which are pump rate and differential pressure. Note that a constant temperature of 190 °F was used for all experiments. No calculations are required for establishing temperature.

2.2.1. Jetting Velocity

The jetting velocity corresponds to the velocity of the fluid when it exits the nozzle. Equation 5 shows the relationship of jetting velocity with the pump rate and the cross-sectional area of the nozzle.

$$v_{jet}=\frac{Q_{pump}}{A_{nozzle,i}}=\frac{Q_{pump}}{\frac{\pi D_{nozzle,i}^2}{4}} \quad (5)$$

Where v_{jet} is jetting velocity, Q_{pump} is pump rate, A_{nozzle} is cross-sectional area of the nozzle, and D_{nozzle} is nozzle diameter. Equation 5 can be rearranged to calculate the

pumping rate required to achieve a specific jetting velocity when using a determined nozzle size, as shown in Equation 6.

$$Q_{pump} = v_{jet} \frac{\pi D_{nozzle,i}^2}{4} \tag{6}$$

In this study, two nozzle sizes were used, 0.0225-inch and 0.019-inch. The pump rates estimation for a jetting velocity of 65 ft/s and the two nozzle sizes are presented below.

$$Q_{pump,1} = \left(65 \frac{ft}{s}\right)\left(\frac{0.0225^2 \pi}{4}\right)\left(\frac{ft^2}{144\ in^2}\right)\left(\frac{28316.8\ mL}{ft^3}\right)\left(\frac{60\ s}{min}\right) \tag{7}$$

$$Q_{pump,1} = 304.93 \frac{mL}{min} \cong \mathbf{305 mL/min} \tag{8}$$

$$Q_{pump,2} = \left(65 \frac{ft}{s}\right)\left(\frac{0.019^2 \pi}{4}\right)\left(\frac{ft^2}{144\ in^2}\right)\left(\frac{28316.8\ mL}{ft^3}\right)\left(\frac{60\ s}{min}\right) \tag{9}$$

$$Q_{pump,2} = 217.4 \frac{mL}{min} \cong \mathbf{217 mL/min} \tag{10}$$

It is recommended verifying the pump rate after the desire differential pressure across the core is established to prevent errors in the experimental conditions. Details of the procedure to verify the pump rate are presented in the procedure section for the acid jetting test.

2.2.2. Differential Pressure

The differential pressure across the core is used to control the interstitial velocity of acid jetting experiments. Interstitial velocity is a term utilized to characterize flow rates through a porous cross-sectional area (Buijse and Glasenbergen 2005; Furui et al. 2010). It is defined as:

$$v_i = \frac{Q}{A\emptyset} \tag{11}$$

Where v_i is interstitial velocity, Q is volumetric flow rate, A is cross-sectional flow area, and $\emptyset$ is porosity. Solving Equations 3 and 6 for Q, and rearranging for ΔP, results in Equation 12, which provides an approximation of the differential pressure needed to create a define interstitial velocity.

$$\Delta P = 607.92 \frac{v_i \emptyset L \mu}{k} \tag{12}$$

Where ΔP is differential pressure across the core in psi, v_i is interstitial velocity in cm/min, L is core length in inches, μ is viscosity in cp, k is permeability in mD. The conversion factor 607.92 for obtaining the differential pressure in psi is presented below. In practice, the differential pressure from this calculation is used to set the upstream and downstream pressures properly.

$$\frac{1\frac{cm}{min}\left(\frac{min}{60\ s}\right)\left(\frac{0.01\ m}{cm}\right)1in\left(\frac{0.0254\ m}{in}\right)1\ cp\left(\frac{0.001\ Pa-s}{cp}\right)}{1mD\left(1.01\times10^{-15}\frac{m^2}{mD}\right)}\left(1.45\times10^{-4}\frac{psi}{Pa}\right)=607.92 \quad (13)$$

2.3. Acid jetting experiment

This section presents the experimental apparatus and procedure for the jetting core-flood tests.

2.3.1. Experimental Apparatus

The acid jetting experimental apparatus consists of a pumping system, a 4-in core holder, a heating system, pressure regulators, a flow control system, and the data acquisition hardware. The pumping system includes a pulse pump and two storage tanks for acid and water. The heating system consists of a water bath with two immersible-electrical heaters and a heating tape for the lines outside the water bath. Inside the water bath, a ½-inch coiled tubing section of 190-ft in length is placed to allow the flowing fluid to reach the desired temperature. The upstream and downstream pressures are controlled by two back-pressure regulators, each connected to individual nitrogen tanks that enable differential pressure manipulation. The control system includes an actuator-control valve combo and a high-precision weight scale, which feeds real-time data to LabVIEW, allowing constant interstitial velocity tests. The data acquisition hardware includes two type k thermocouples, a differential pressure transmitter, and a computer. The incoming data from the weight scale, pressure transmitter, actuator-control valve, and the

thermocouples are gathered in a LabVIEW program. Figure 5 shows a schematic of the experimental apparatus for acid jetting tests.

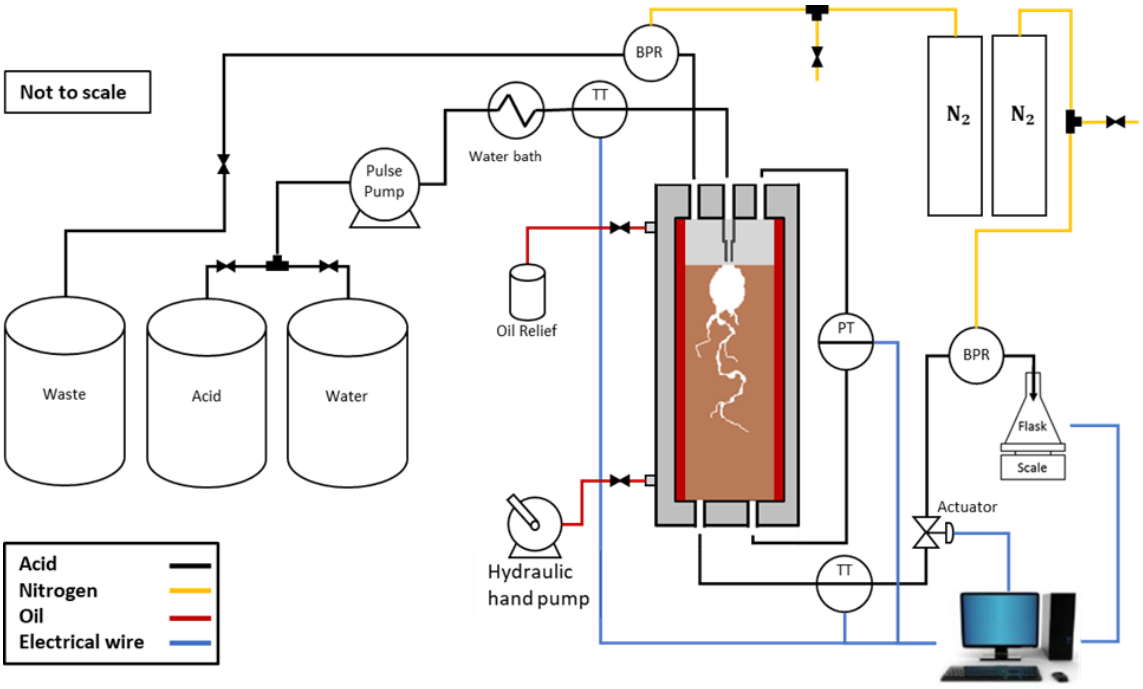

Figure 5. Acid jetting experimental setup for constant interstitial velocity condition

The injection pump is a Chem/Meter 802 pulse pump, rated for 1,000 ml/min and 1,900 psi maximum operating conditions. The pump intake is connected to the water and acid tanks, and the outlet of the pump is connected to the heating system, which is subsequently connected to the 4-inch core holder.

Figure 6 shows a schematic of the 4-inch core holder (Ridner 2018), including the main parts of the core holder itself, as wells as the inlet and outlet lines. The inlet cap (Figure 6 top) consists of three lines, the inlet line, upstream pressure, and return line. The inlet line receives the fluid from the injection pump. A nozzle was attached at the tip of the inlet line, which allows the fluid velocity to increase when it exits the nozzle. Note

that spacer rings were used to establish a distance between the nozzle tip and the sample face; this distance is known as stand-off distance. This distance was constant throughout this study. The upstream pressure line is connected to the differential pressure transmitter, and the return line enables the fluids that are not flowing through the rock to be relieved from the system. In addition, the return line is connected to a back-pressure regulator, allowing the user to set a specific pressure on the system.

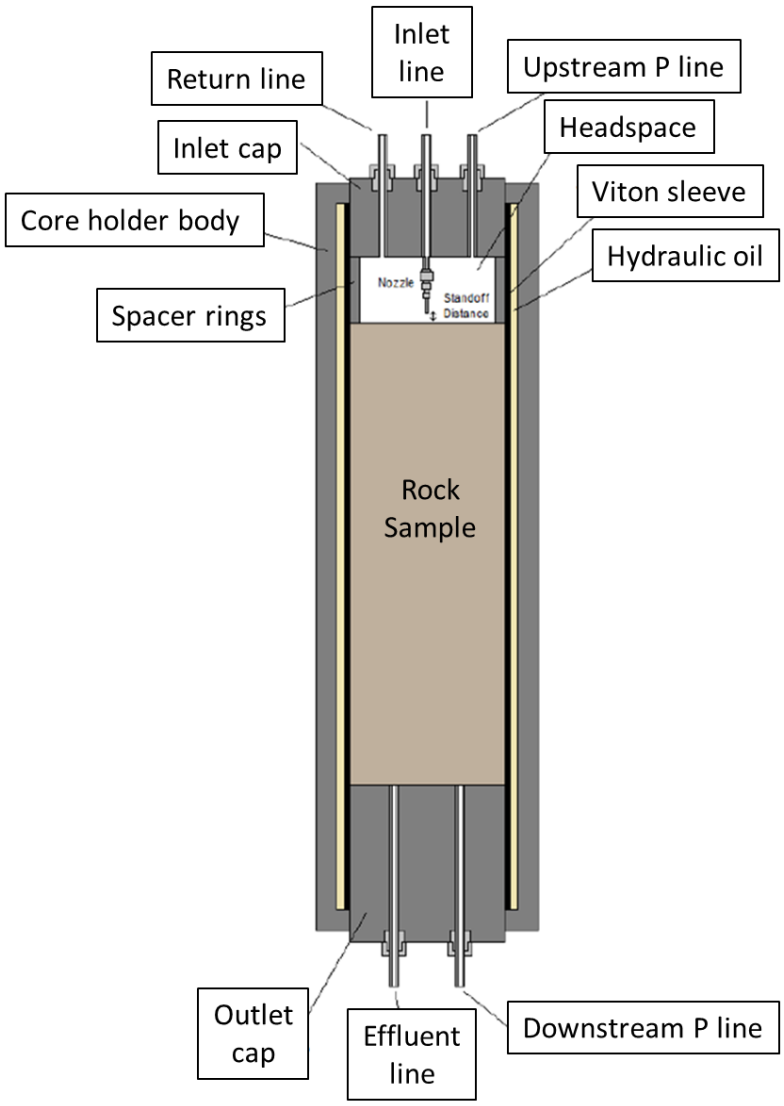

Figure 6. Schematic of the acid jetting core holder (Reprinted from Ridner (2018))

As shown in Figure 6, a Viton sleeve is used to isolate the core sample from the hydraulic oil pumped for increasing the confining pressure. In addition, Figure 6 presents the outlet cap (Bottom) with two lines, the downstream pressure line, and the effluent line. The downstream pressure line is connected to the differential pressure transmitter. The effluent line connects the outlet of the core holder to the control valve, which is also connected to the downstream back-pressure regulator. Finally, the effluent line connects to a flask on top of the weight scale. The downstream back-pressure regulator was set to 1,000 psi for all experiments. The differential pressure was obtained by manipulating upstream pressure only.

The control valve and weight scale are presented in Figure 7; these elements transmit valve position and weights to a LabVIEW program, respectively. The data from these elements is acquired every 0.5 seconds. The control valve allows the user to adjust the valve position, generating a choking effect on the effluent line, if required. From the weight scale readings over time, a mass flow rate is estimated. Then, based on the assumption that the density of the effluent is approximately equal as that of water (1 g/mL), a volumetric flow rate is calculated by multiplying the mass flow rate and the effluent density. The interstitial velocity is calculated using Equation 11, where the porosity and area are user inputs. Note that the displayed interstitial velocity in the LabVIEW interface represents a moving average of 100 points. This removes fluctuations due to noise and allows the user to visualize more accurately the flowing conditions of the experiment.

Figure 7. Control valve-actuator combo (left) and weight scale and display (right)

2.3.2. Experimental procedure

First, a coiled tubing section of ½-inch in diameter and 190-ft in length was placed inside the water bath with the immersible heaters set to the desired experimental temperature (190 °F). It is recommended to turn on the heating system at the beginning of the assembling process to allow the water bath sufficient time to reach the desired temperature. The saturated and labeled core was then placed inside the core holder body from one end (Figure 8a). The 2-inch and ¼ -inch spacer rings (Figure 8b) were placed flush with the core from the inlet side of the core holder (Figure 8a). Then, the inlet cap was pushed flush with the spacers and then rotated to be secured into place. Note that the nozzle is attached at the end of the inlet cap (Figure 8b). The outlet cap (Figure 8a) was

placed inside the core holder and pushed flush with the sample; then, it was secured into place using the component presented in Figure 8a at the core holder end. The core holder was oriented with the inlet side pointing upwards and the outlet side pointing downwards. Then, all tubing connections between the core holder and the different components of the apparatus were adequately fastened. Once the flow lines were connected, the hand pump was used to pump hydraulic oil into the core holder to increase the confining pressure to 500 psi. Note that the confining pressure varies throughout the test, and has to be maintained 500 psi above the upstream pressure to ensure flow through the core and not around it. Due to the elevated temperature of the tests, the hydraulic oil expands, and the confining pressure increases. It is recommended to verify that the confining pressure is in the desired range to prevent excessive radial pressure onto the core.

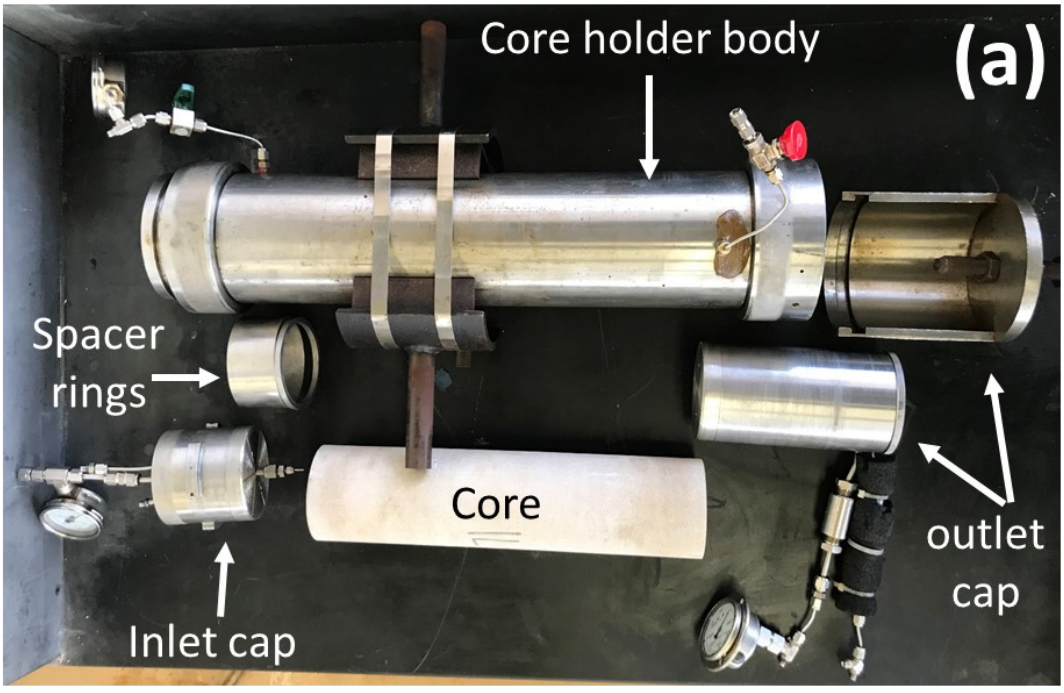

Figure 8. (a) Core holder parts and (b) Inlet cap components

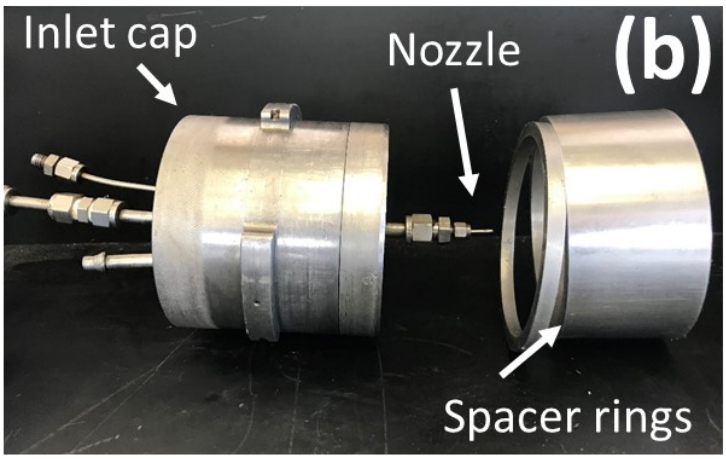

Figure 8 Continued.

Once the core holder was set up, and all flowlines were fastened, the acid was placed in the acid storage tank. Following acid placement, the required flow parameters, porosity, sample dimensions, and desired interstitial velocity, were included in the LabVIEW interface presented in Figure 9. Then, the water pre-flush was initiated, and the program was started by clicking the arrow bottom on the top left corner of the interface (Figure 9).

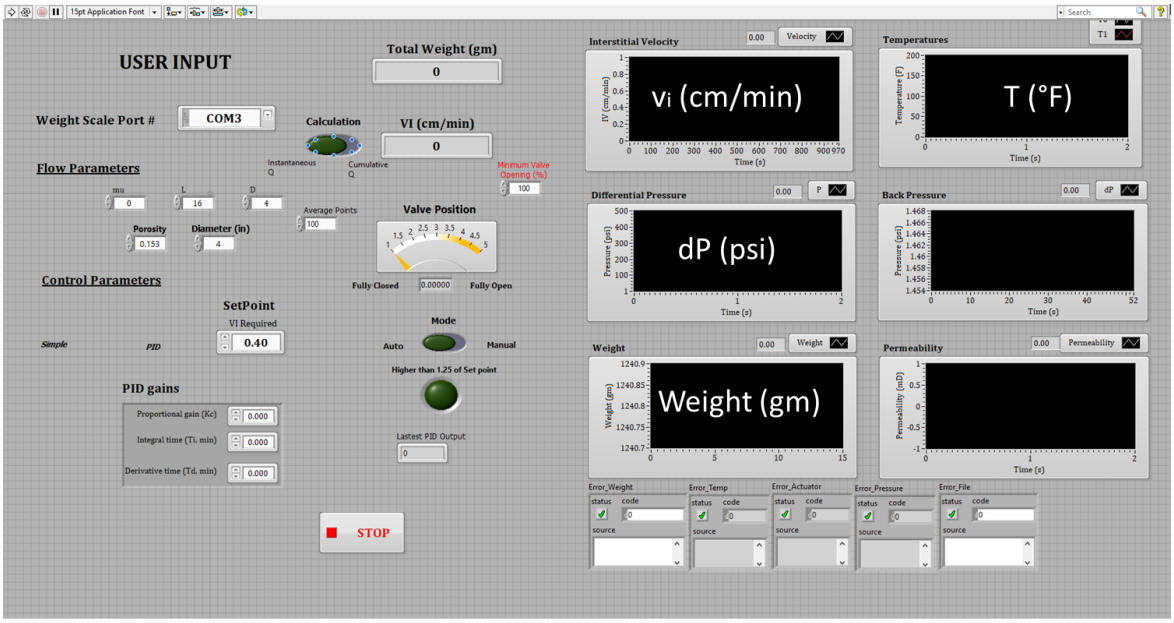

Figure 9. LabVIEW Interface for Acid Jetting Experiments

During water pre-flush, pressure increments of 250 psi were performed in both upstream and downstream back-pressure regulators, until 1,000 psi was reached. This pressure is required to prevent the change of state of carbon dioxide (CO2), which is produced in the acid and rock chemical reaction. After each increase, the differential pressure across the core was allowed to equalize before performing the next pressure increase. Once both upstream and downstream pressures were 1,000 psi, the differential pressure to create flow across the core at the desire matrix flux was established by increasing the upstream pressure only. Note that the differential pressure estimated in section 2.2.2 was used as a guideline for setting the upstream pressure. In practice, the downstream pressure was set to a constant value of 1,000 psi. Then, the upstream back-pressure regulator was set to approximately 1,075 psi, and small increments were performed while monitoring the differential pressure and the interstitial velocity in LabVIEW.

Once the matrix flow rate was correctly established at testing conditions, the jetting velocity was verified by measuring the flow rate of the pump. This was performed by redirecting all the injected water to the returning line and measuring the flow rate with a graduated cylinder. For accurate results, it is recommended to verify the pump rate at the upstream pressure that allows the desired matrix flux. This, considering that the pulse pump flow rate is reduced by increasing the upstream pressure. The empirical correlation presented in Equation 13 (Ridner, 2018; Frick, 2018) shows the inverse dependence of flow capacity to upstream pressure. In this study, it was used to estimate the initial value of pump capacity for the specific experimental conditions. In practice, pump capacity

requires slight trial and error manipulation to obtain the estimated flow rates calculated in section 2.2.1.

$$capacity\ \% = 0.004554 \frac{v_{jet}}{\left(1 - \frac{P_{upstream}}{1950}\right)} \tag{14}$$

Where $P_{upstream}$ is pressure in psi, and v_{jet} is jetting velocity in ft/s. In this study, the jetting velocity values were 150 ft/s, 65 ft/s, and 25 ft/s.

After establishing the correct pump and matrix flow rates, the fluid temperature was verified to be constant. In this study, a variation of +/-2 °F from the ideal temperature was allowed. Once the desired temperature and flow conditions were verified, the injection fluid was switched from water to acid. This was performed via two ball valves that allow the acid and water tanks to be connected to the inlet of the pulse pump.

In this study, the jetting time was calculated as the time elapsed between the valve switch from water to acid, and the valve switch from acid to water. However, the acid only reaches the core face after displacing the water inside the flow lines. The displacement time of the fluid from the pump to the nozzle tip depends on the pump rate. It is essential to consider this time as from that moment, the acid jetting portion of the experiment is initiated. The injection line nominal volume of this study was 1,059 mL, and depending on the pump rate, the displacement time ranged from 1.5 min to 9 min. For data analysis, the displacement time was added to the valve switches to determine the time period in which the rock was in contact with the acid jet.

As the water was displaced in the flowlines, and acid reached the nozzle tip, the acid jet started to contact the core. Previous experimental work shows that cavity growth and wormhole propagation are initiated as acid jetting begins (Holland 2014, Ndonhong 2014, Belostrino 2016, Frick 2018, Ridner 2018). As the rock is dissolved, the length of the core is virtually reduced, assuming that the flow through the wormholes and cavity have negligible pressure drop compared with the flow through the rock matrix. This apparent length reduction decreases the restriction to the fluid to flow through the core sample and increases the interstitial velocity as wormholes propagate, and cavity grows.

The control valve-actuator combo enables the experimental apparatus to control the differential pressure variation as it controls the needle valve position from fully open (100%) to fully closed (0%). As the valve closes, it generates a choking effect at the downstream face of the core, reducing the differential pressure across the core, and hence stabilize the interstitial velocity. The valve was not allowed to be fully closed as it would prevent the fluid from flowing through the core. The LabVIEW program allows two options to communicate and control the valve position, (1) through a proportional-integral-derivative function or (2) manual input from the user. In this study, the second method was used due to its simplicity and consistency in controlling interstitial velocity. The needle valve was closed in 1% to 2% decrement until the desired interstitial velocity was achieved.

Acid breakthrough was prevented by monitoring the differential pressure. Once the jetting time elapsed, the ball valves were switched back to water injection, and the water post-flush was initiated, maintaining constant experimental conditions. The water post-

flush lasted until water displaced the remaining acid in the system; this was monitored by measuring the pH of the returning line fluid and effluent. This step of the procedure allows all the pumped acid to reach the core, and it also helps to quantify the exact volume of acid used throughout the test.

After a pH of 7 was measured in both ends, the pressures were relieved, the pump was shut down, flowlines were disconnected, the core holder inlet and outlet caps were removed, and the core was removed from the core holder. The core was then scanned for 3D characterization of the dissolution structure. The last step in the experimental procedure was to dry the core sample in the oven for 24 hours at 110 °F and then weigh it to determine the mass of rock dissolved during the experiment.

2.4. Sample imaging and 3D visualization

After the acid portion of the experiment, each core was scanned in a Toshiba Aquilon TSX-101A/RG X-ray CT machine, shown in Figure 10.

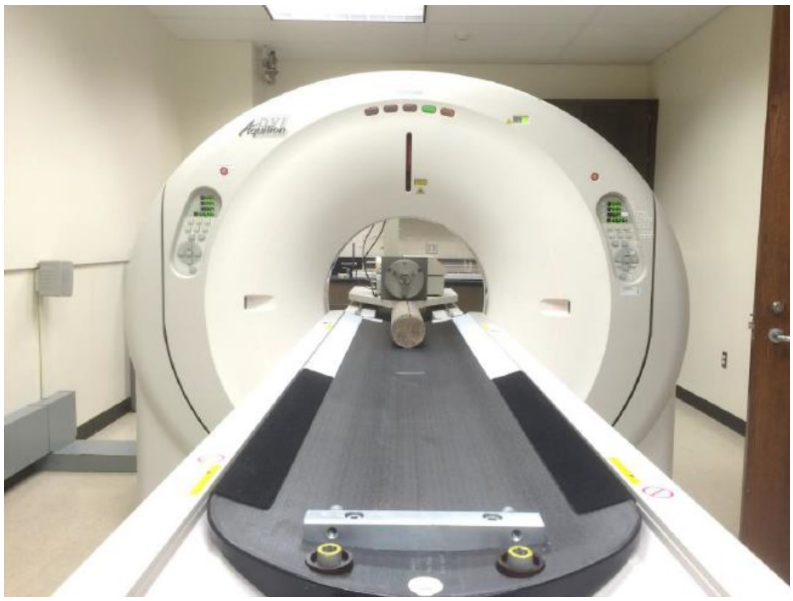

Figure 10. Toshiba Aquilon CT scanner

The imaging process provides a 3D visualization of the dissolution structures created by the acid jetting test. Measurements of cavity and wormholes dimensions are allowed within the image processing. The CT machine scan cross-sectional slices of the core with a thickness/resolution defined by the user. In this study, a resolution of 0.5 mm was used for the 3D visualization and to estimate the dissolution structure dimensions. After scanning, the raw DICOM data was retrieved using ImageJ and processed by using a medical software, called Horos™. This software allows the user to manipulate two ranges of pixel values for volume rendering (Figure 11), one representing the bulk material and one representing the void space. This was used to identify the dissolution patterns. See Appendix A for a step-by-step procedure on image processing.

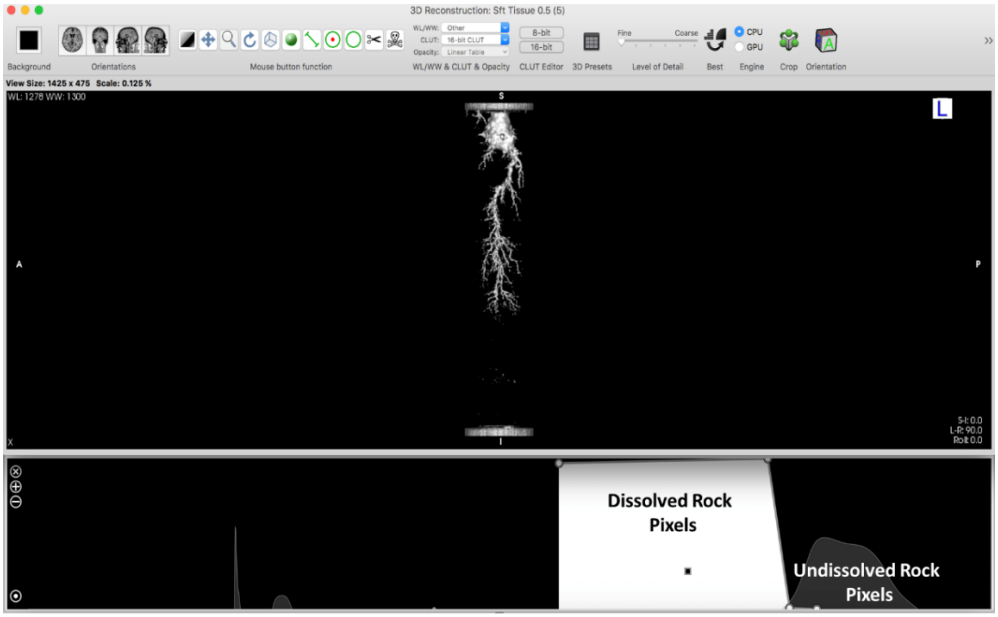

Figure 11. 3D volume rendering of the dissolution structure

Through the built-in functions of Horos™, the dissolution pattern features were characterized. Figure 12a shows the measurement feature used for estimating wormhole length and cavity depth. Figure 12b presents the calculation of cavity volume. A similar procedure was used to estimate the total dissolved volume (wormholes and cavity). The 3D visualization and characterization of the dissolution structure allow the user to quantitative compare different experiments. Horos™ also enables the user to produce a video of the dissolution pattern rotating around the central axis of the core; this was performed for all samples for improving visualization.

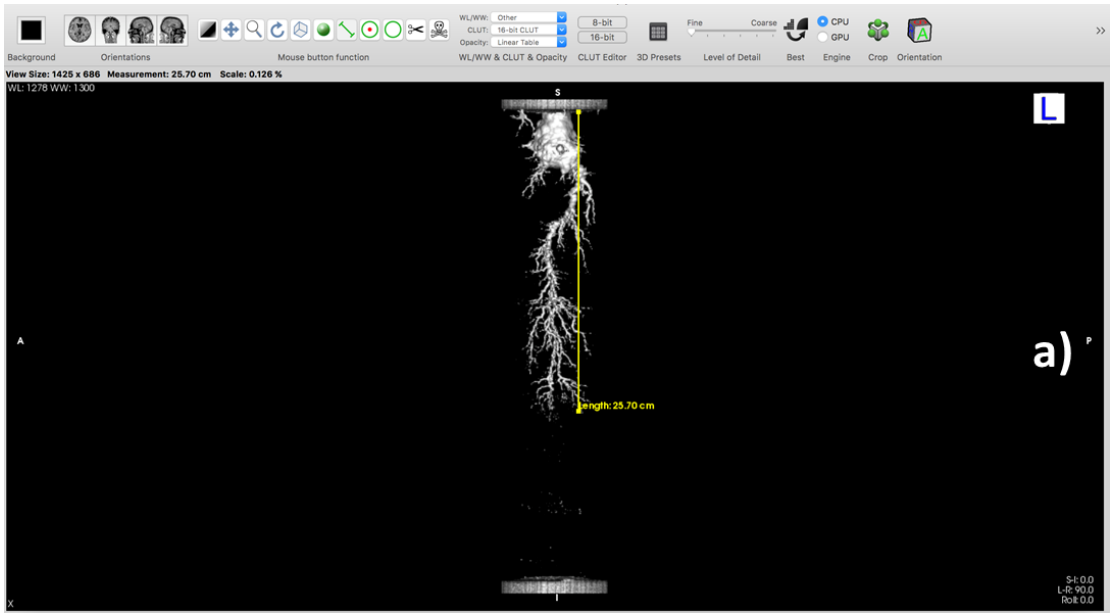

Figure 12. Horos™ software built-in functions a) Wormhole length measurement. b) Cavity volume calculation

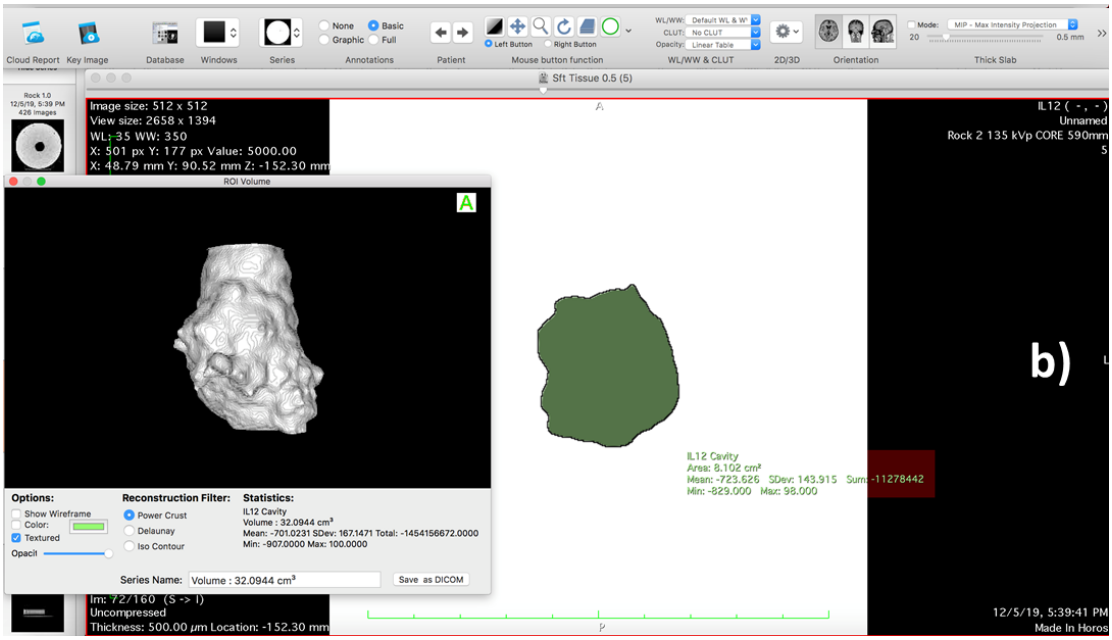

Figure 12 Continued.

2.5. Modified Acid System

The modified acid system was design based on the concept of Lewis acid-base reaction, which results in a coordinate covalently bonded compound, also known as adduct. The theory of the Lewis acid-base reaction is presented in Equation 15, where A is the Lewis acid that accepts an electron pair, B is the Lewis base that donates an electron pair, and A-B is the adduct product.

$$A^+ + B^- \rightarrow A - B \tag{15}$$

The modified acid system has two main components in terms of volume and weight percent of the composition, Lysine, and HCl, in molar ratios ranging from 1:3 to 1:12.5; metal iodides or iodates, and alcohols are also included in the modified acid for corrosion inhibition purposes (Purdy et al. 2018). The Lysine (C6H14N2O2) is an amino acid that

contains at least one amino group -NH2, and one carboxyl group, -COOH (Figure 13), these compounds act as the Lewis base, and the HCl acts as Lewis acid.

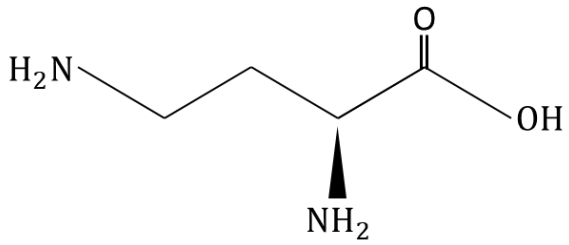

Figure 13. Lysine Chemical Structure

By adding together Lysine and HCl, a Lewis adduct is formed. The Lysine neutralizes the HCl at a molar ratio up to 1:2. However, at molar ratios above 1:2, the Lysine reduces the solubilizing ability of the acid without neutralizing it. This adduct produces a controlled reaction rate of the HCl with carbonate material. This effect is due to the stronger molecular bonds of the adduct compare to HCl molecular bonds. In addition, the Lysine:HCl adduct has reduced hazardous effects when compared with HCl, and it also adopts the biodegradable properties of Lysine, resulting in an environmentally friendly stimulation fluid.

The modified acid system is patented for a variety of molar ratios, which can be manipulated depending on the solubility requirements for a specific formation rock. Purdy et al. (2018) presented experimental results regarding the performance of the modified acid, including corrosion testing, dissolution testing, matrix acidizing, fluid stability, compatibility, the effect on human health, among others. Matrix acidizing results using Indiana limestone samples suggest that the modified acid (molar ratio 1:4.5) provides

higher stimulation efficiency compared to 15% HCl, especially at lower injection rates. It was observed that the modified acid resulted in lower optimal interstitial velocity and similar optimal pore volumes to breakthrough, compared to 15% HCl. In addition, due to the controlled reaction rate of the modified acid, for injection rates below the optimal conditions, the wormhole diameters were found to be similar to the observed in the optimal condition. On the contrast, when using 15% HCl, compact dissolution was observed at injection rates below the optimal condition. In this study, a modified acid system of 90% Lysine:HCl composition in a molar ratio of 1:4.5 is tested for wormholing efficiency under jetting conditions for carbonate reservoirs.

3. RESULTS AND DISCUSSION

This section presents and discusses 21 acid jetting experiments performed on Indiana Limestone cores at 190 °F. The modified acid was used for 15 tests, and 15% HCl was used in 6 tests. The experiments are grouped by sets according to the variable investigated in the group, as shown in Table 2. In addition, Table 2 presents the experimental conditions for all the tests performed and evaluated in this study. The experiments labeled as IB were taken from Ridner et al. (2020) for comparison purposes. Note that compared to the initial samples of Table 1, samples IL1, IL7, IL8, and IL9, are not included in the data sets presented in Table 2. This, considering that the experimental conditions were not constant during the jetting tests, or the experiment was not comparable with others. The details and lessons learned from these experiments are presented in section 3.4. It is important to note that experiments at a jetting velocity of 150 ft/s were performed following the experimental procedure of the previous 15% HCl. In these last experimental studies, the pumping rate used to derive the jetting velocity was assumed to be constant at the initial and final upstream pressures. In practice, the flow rate of the pump is reduced as the upstream pressure increases to its last set point, resulting in a reduction of the experimental jetting velocity. For experiments at a jetting velocity of 65 ft/s and 25 ft/s, the pump rate was verified after the upstream pressure was set to the final condition, at which the desired interstitial velocity was achieved. Appendix B presents all the experimental results and comparison metrics for all the experiments analyzed in this section.

Table 2. Summary of experimental conditions for all data sets

Experiment Number	Set	Interstitial Velocity (cm/min)	Jetting Velocity (ft/s)	Jetting Time (min)	Nozzle Size (in)	Acid System
IL15	Baseline	0.2	65	16.10	0.0225	Modified Acid
IL16		0.4		15.73		
IL11		0.71		15.81		
IL5	Increased Jetting Velocity / Low Jetting Time	0.2	150	16.10	0.0225	Modified Acid
IL6		0.4		15.50		
IL4		0.73		15.76		
IL19	Decreased Jetting Velocity	0.2	25	15.78	0.0225	Modified Acid
IL18		0.4		15.93		
IL17		0.71		15.81		
IL13	Decreased Nozzle Size	0.2	65	15.73	0.0190	Modified Acid
IL14		0.4		15.90		
IL12		0.71		16.36		
IL10	Increased Jetting Time	0.2	150	37.31	0.0225	Modified Acid
IL2		0.4		37.33		
IL3		0.73		40.30		
IL20	Baseline HCl	0.2	65	15.85	0.0225	15% HCl
IL21		0.4		15.85		
IL22		0.7		15.71		
IL23	Decreased Jetting Velocity HCl	0.2	25	15.95	0.0225	15% HCl
IL24		0.4		0.00		
IL25		0.7		0.00		
IB15*	Increased Jetting Velocity HCl	0.2	150	16.10	0.0225	15% HCl
IB13*		0.4		15.00		
IB14*		0.74		15.30		

* High-temperature experiments presented by Ridner et al. (2020).

3.1. Evaluation Metrics for Acid Jetting

In matrix acidizing experiments, the acid is pumped at a constant rate until a wormhole breaks through the core. Thus, for matrix acidizing tests, there are only one inlet and one outlet from the core holder. This allows the acid flowing through the core to be equivalent to the effluent flowing out of the rock. The dimensionless parameter Pore Volumes to Breakthrough (PV_{bt}) is used for measuring the treatment efficiency.

PV_{bt} represents the volume of acid needed to propagate a wormhole through the core, where a lower PV_{bt} represents a more efficient treatment. PV_{bt} can be calculated with the following Equation:

$$PV_{bt} = \frac{V_{acid}}{V_{pore}} = \frac{V_{acid}}{\frac{\pi}{4} D_{core}^2 L_{core} \emptyset} \quad (16)$$

Where V_{acid} is the volume of acid required to dissolve. If the propagated wormhole front does not break through the entire core, Equation 16 can still be used by substituting the length of the core by the length of the wormhole. The wormhole length is obtained from the 3D image processing. This dimensionless parameter can be plotted against the interstitial velocity in a log-log scale to generate a wormhole efficiency plot.

In acid jetting experiments, there are two velocities defined. The acid flowing from the pump through the nozzle creates the jetting velocity, which represents the high-velocity acid stream impacting the rock. Then, flow across the core is generated by applying a differential pressure, which represents the interstitial velocity, i.e., volume of acid flowing through a porous cross-sectional area. Note that the injection rate needed to achieve the high-velocity jet through the nozzle is always higher than the matrix flow rate. As a result, not all the injected acid flows through the rock, and the excess of acid must be evacuated from the system to have constant differential pressure along the entirety of the acid jetting test. Figure 14 presents a schematic of the flow path differences between matrix acidizing and acid jetting, where the red arrows represent the acid flow path.

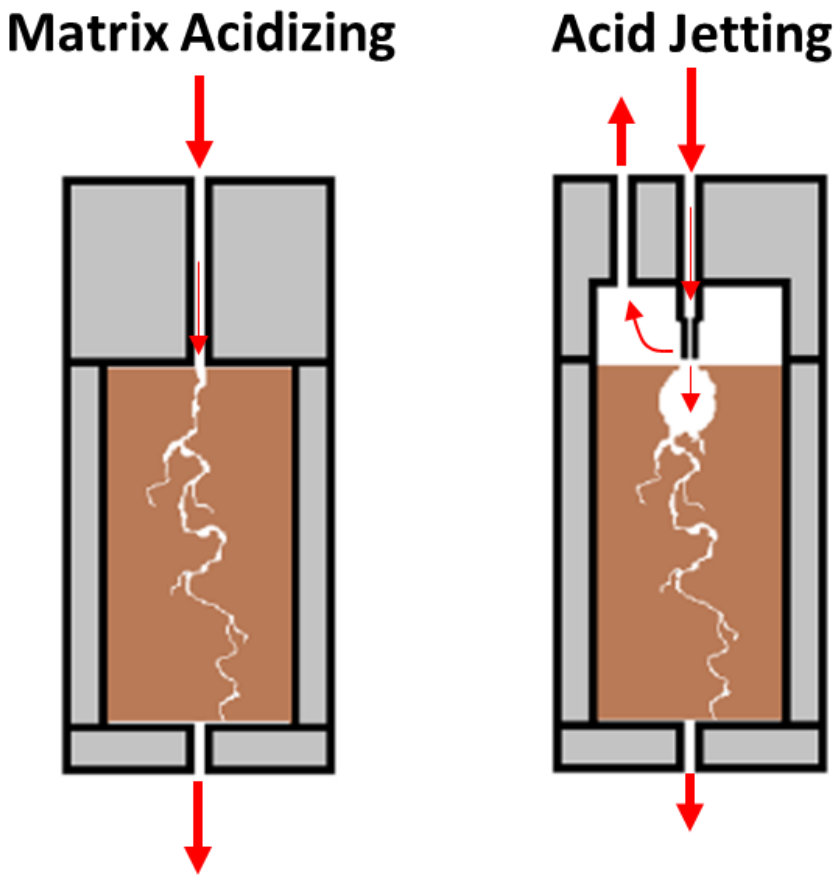

Figure 14. Flow path comparison between matrix acidizing and acid jetting experiments

Figure 14 presents a fundamental problem for evaluating acid jetting efficiency following the matrix acidizing method. Note that matrix acidizing allows only one flow path through the matrix of the core. However, in acid jetting, a small volume of acid is allowed to flow through the core, and a larger volume is evacuated through a returning line. In this study, three calculation methods were assessed to quantify acid jetting results. The first one considers the volume of acid required to propagate a wormhole to a specific length using the effluent; thus, only matrix flow is considered as in matrix acidizing. The second method accounts for the acid volume needed to dissolve the rock volume occupied

by the cavity and wormholes. In matrix acidizing, these two values would be equal since the injected flow, and the affluent are the same; however, for acid jetting, these flow values are different. Appendix D shows a calculation comparison between both methods. The third method is used as a comparison metric between the tests, but it does not intend to measure efficiency.

Table 3 shows the matrix acidizing experiments performed by Ridner (2018) that are used to compare the PV_{bt} resulted from matrix acidizing and acid jetting. These experiments were performed using 15% HCl, and Indiana limestone cores of 4-inch in diameter and 16-in in length. This comparison is not intending to compare the values of PV_{bt}, but the different behaviors observed in both experiments. Samples IL20, IL21, and IL22 were used for the acid jetting experiments.

Table 3. Matrix acidizing experiments

Experiment Number	Porosity (%)	Permeability (mD)	Interstitial Velocity (cm/min)	Jetting Time (min)	Wormhole Length (cm)	PVbt
1	15.2%	2.3	0.29	56.6	11.90	1.38
2	15.3%	3.3	0.67	17.0	24.30	0.47
3	15.1%	2.5	1.16	7.0	16.63	0.49

3.1.1. PV_{bt} Based on Effluent Flow

This method calculates the pore volumes to breakthrough considering the volume of acid flowing through the core; therefore, it accounts for the acid spent in wormhole propagation only. The volume of acid in Equation 16 can be calculated by solving Equation 6 for flow rate and multiplying it by the jetting time, resulting in the PV_{bt} estimation presented in Equation 17. The v_i used in Equation 17 is obtained by

averaging the interstitial velocity values recorded in LabVIEW during the acid jetting portion of the test.

$$PV_{bt} = \frac{v_i t_{jet}}{L_{wh}} \tag{17}$$

Where v_i is the average matrix flux in cm/min, t_{jet} is the jetting time in min, and L_{wh} is the wormhole length in cm. Note that L_{wh} considers the length of the wormhole from the base of the cavity to the tip of the wormhole. This PV_{bt} calculation method presents limitations when estimating acid jetting efficiency as it does not consider the acid spent in cavity formation.

Figure 15 presents the PV_{bt} results for the matrix acidizing experiments presented in Table 3, and samples IL20, IL21, and IL22 for acid jetting. The fit of the matrix tests was performed using the Buijse and Glasenbergen (2005) model. Note that the behavior of PV_{bt} for the acid jetting differs from the matrix acidizing tests. For matrix acidizing, an optimal injection condition is observed, and the efficiency is lost rapidly below that optimal injection condition. However, for acid jetting, the efficiency increases as the interstitial velocity decrease. This method to estimate PV_{bt} assumes that all the injected acid flows through the core, and this is only true for matrix acidizing tests. Thus, this PV_{bt} calculation method does not represent the efficiency of acid jetting tests.

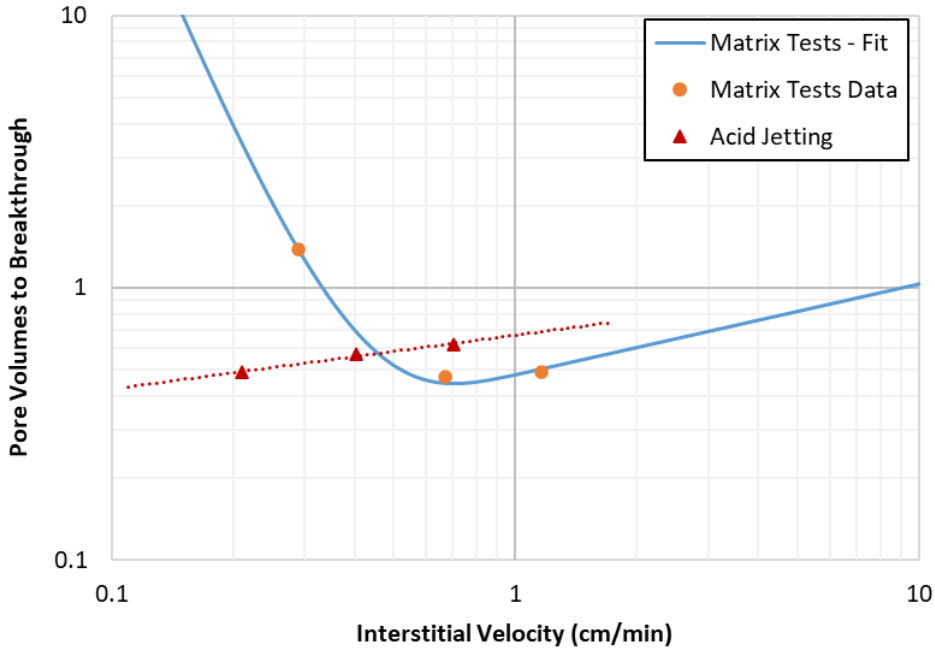

Figure 15. Matrix acidizing and acid jetting PV_{bt} – Based on effluent flow

3.1.2. PV_{bt} Based on Dissolved Rock Volume

This method considers the volume of acid required to dissolve the rock occupied by the cavity and wormholes in the core. The calculation is based on the acid dissolving power, x, which is a dimensionless parameter that represents a volume of mineral dissolved per volume of acid solution (Zhu, and Furui, 2018). Equations 18 and 19 represent the dissolving power calculations.

$$x = \beta\left(\frac{\rho_{acid\ solution}}{\rho_{mineral}}\right) \tag{18}$$

$$\beta = \frac{v_{mineral}MW_{mineral}}{v_{acid}MW_{acid}} \tag{19}$$

Where x is the volumetric dissolving power, β is the gravimetric dissolving power, $\rho_{acid\ solution}$ is the density of the acid solution, $\rho_{mineral}$ is the density of the reacting mineral, $v_{mineral}$ and v_{acid} are the stoichiometric constants from the acid-mineral reaction, and $MW_{mineral}$ and MW_{acid} are the molecular weights of the mineral and acid. Considering Indiana limestone mineralogy, it can be assumed that the reaction kinetics is strictly defined between acid system and $CaCO_3$. The reaction between HCl and CaCO3 is the following:

$$2HCl + CaCO_3 \rightarrow CaCl_2 + CO_2 + H_2O \tag{20}$$

From the stoichiometric reaction, the parameters for Equation 18 can be obtained. Due to privacy policies, the chemical composition of the modified acid was not provided by the service company. Thus, the dissolving power of both acid systems, 15% HCl and the modified acid, was assumed to be equal. The dissolving power was calculated for 15% HCl and Indiana Limestone, as follows:

$$\beta_{100} = \frac{1 \times 100.1}{2 \times 36.6} = 1.37 \frac{g\ CaCO_3}{g\ HCl} \tag{21}$$

$$\beta_{15} = 0.15 \times \beta_{100} = 0.21 \frac{g\ CaCO_3}{g\ HCl} \tag{22}$$

$$x_{15} = \beta_{15}\left(\frac{\rho_{acid\ solution}}{\rho_{mineral}}\right) = 0.21\frac{g\ CaCO_3}{g\ HCl}\left(\frac{1.07\frac{g\ HCl}{cm^3\ HCl}}{2.71\frac{gCaCO_3}{cm^3\ CaCO_3}}\right) \quad (23)$$

$$x_{15} = 0.0829\frac{cm^3\ CaCO_3}{cm^3\ HCl} \quad (24)$$

After calculating the dissolving power for both acid systems with Indiana Limestone, the volume of rock dissolved was required to estimate the acid spent in the dissolution process. In this study, the dissolved rock volume was assessed using two different methods. The first method considers the core's dry mass change and the mineral density to estimate the volume CaCO3 dissolved, as presented in Equation 25.

$$V_{CaCO_3,dissolved} = \frac{m_{dry,initial} - m_{dry,final}}{\rho_{CaCO_3}} \quad (25)$$

Where $V_{CaCO_3,dissolved}$ is the volume of calcium carbonate dissolved during acid jetting, $m_{dry,initial}$ and $m_{dry,final}$ are the dry masses before and after the acid jetting test, and ρ_{CaCO_3} is mineral density. This calculation method may present accuracy limitations in core samples where material losses non-related to the acid jetting test occurred. These material losses can happen at the edges of the samples due to high confining pressure.

The second method used to estimate the CaCO3 dissolved volume uses the CT image processing methodology described in section 2.3. However, this volume corresponds to the bulk dissolved volume, and it is critical to adjust it by accounting for the pore volume within the total volume of rock dissolved, as presented in Equation 26.

$$V_{CaCO_3,dissolved} = V_{CaCO_3,bulk}(1 - \emptyset) \quad (26)$$

Where $V_{CaCO_3,dissolved}$ is the net volume of calcium carbonate dissolved during acid jetting, $V_{CaCO_3,bulk}$ is the bulk volume of calcium carbonate dissolved (directly from the processing software), and $\emptyset$ is the core's porosity. The CT image results are not affected by non-jetting mass losses, and consistent measurements can be applied between samples. The estimated dissolved $CaCO_3$ in acid jetting can be transformed into the required volume of 15% HCl, as follows:

$$V_{15\%\,HCl} = \frac{V_{CaCO_3,dissolved}}{x_{15}} \quad (27)$$

The PV_{bt} is then calculated following Equation 16. Note that for all experiments in this study, the L_{core} was substituted by L_{wh} as acid did not break through the core. The two methods to calculate the volume of dissolved rock resulted in similar calcium carbonate dissolved volumes and were used as verification for each other.

Figure 16 shows the PV_{bt} results for the matrix acidizing experiments presented in Table 3 using the presented method above. Samples IL20, IL21, and IL22 are used for the acid jetting calculations. The fit of the matrix tests was performed using the Buijse and Glasenbergen (2005) model. Note that even considering the complete dissolved volume, the behavior of PV_{bt} for the acid jetting differs from the matrix acidizing tests. No optimal condition is observed for the acid jetting experiments. This is due to the fundamental

difference in the flow path of the injected fluid from acid jetting and matrix acidizing. Thus, PV_{bt} estimations using this method must be used with caution for acid jetting.

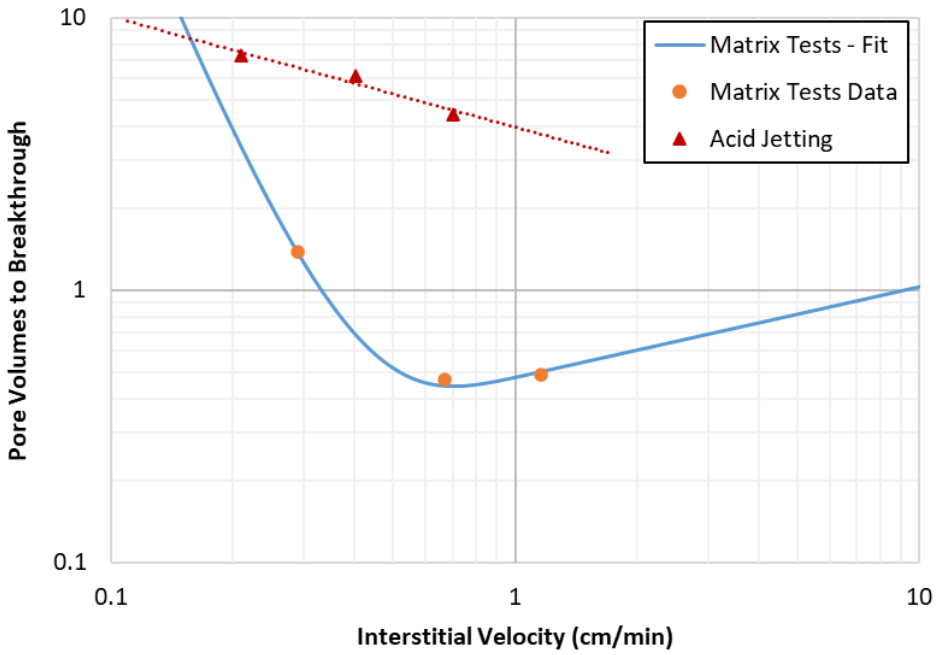

Figure 16. Matrix acidizing and acid jetting PVbt – Based on dissolve rock volume

Considering the PV_{bt} limitations for acid jetting, it was not used as a comparison metric in this study.

3.1.3. Wormhole Propagation Rate

Wormhole propagation rate was used as a comparison metric for acid jetting experiments (Frick, 2018). It was first used in matrix acidizing tests as the length of wormhole through the core over the acidizing time, as presented below.

$$v_{wh} = \frac{L_{wh}}{t_{jet}} \tag{28}$$

This Equation is used similarly for acid jetting and matrix acidizing experiments since it is not dependent on the acid flow path. However, this evaluation method does not refer to the efficiency of the acid treatment. Thus, in this study, an optimal efficiency condition will not be presented. The length of the wormhole in Equation 28 can be replaced by cavity depth or cavity volume to evaluate the cavity growth rate, and cavity enlargement rate, respectively. The cavity growth rate refers to the average depth increase of the cavity during the test, and it is expressed in cm/min. The cavity enlargement rate refers to the average rate at which the cavity volume was increasing during the experiment, and it is expressed in cc/min. The impact of jetting velocity, jetting time, interstitial velocity, and nozzle size is evaluated qualitatively with the 3D dissolution structures and quantitatively using the propagation rates from Equation 28.

3.2. Acid Jetting Results Using a Modified Acid System

This section presents the acid jetting results of a parametric study performed with the modified acid system. This investigation intended to evaluate the effect of increasing jetting time, the impact of nozzle-size variation, and the influence of jetting velocity on the dissolution structures. Appendix E presents the CT scan images for all samples.

3.2.1. Effect of Vary Jetting Time on Dissolution Structures

The impact of jetting time was evaluated by performing experiments with low and high jetting time, which is similar to have low and high injected volumes. Table 4 presents the experimental conditions for the experiments included in this section. Note that the jetting time for the low cases was about 15 minutes, and for the high jetting time cases,

the jetting time was increased to almost 40 min. For each of the data sets, at least one test was performed at an interstitial velocity of 0.2, 0.4, and 0.7 cm/min. Note that the jetting velocity, nozzle size, acid system, and temperature are constant for the experiments in this data sets, only jetting time was varied. The inlet temperature was maintained at 190 °F with a variation of +/- 2 °F during the test.

Table 4. Experimental conditions for jetting time investigation

Experiment Number	Set	Interstitial Velocity (cm/min)	Jetting Velocity (ft/s)	Jetting Time (min)	Nozzle Size (in)	Acid System
IL5	Low Jetting Time	0.2	150	16.10	0.0225	Modified Acid
IL6		0.4		15.50		
IL4		0.73		15.76		
IL10	Increased Jetting Time	0.2	150	37.31	0.0225	Modified Acid
IL2		0.4		37.33		
IL3		0.73		40.30		

Figure 17 presents the CT scan images for all six tests. The interstitial velocity increases from left to right, and the letters L and H in the figure correspond to low and high-volume tests, respectively. As expected, using a higher volume of acid resulted in larger cavities and more extended wormholes for all conditions. However, it is observed that neither the cavity depth nor the wormhole length increased proportionally to the increase of jetting time. A significant portion of the additional acid in the high-volume experiments was spent on cavity enlargement instead of wormhole growth.

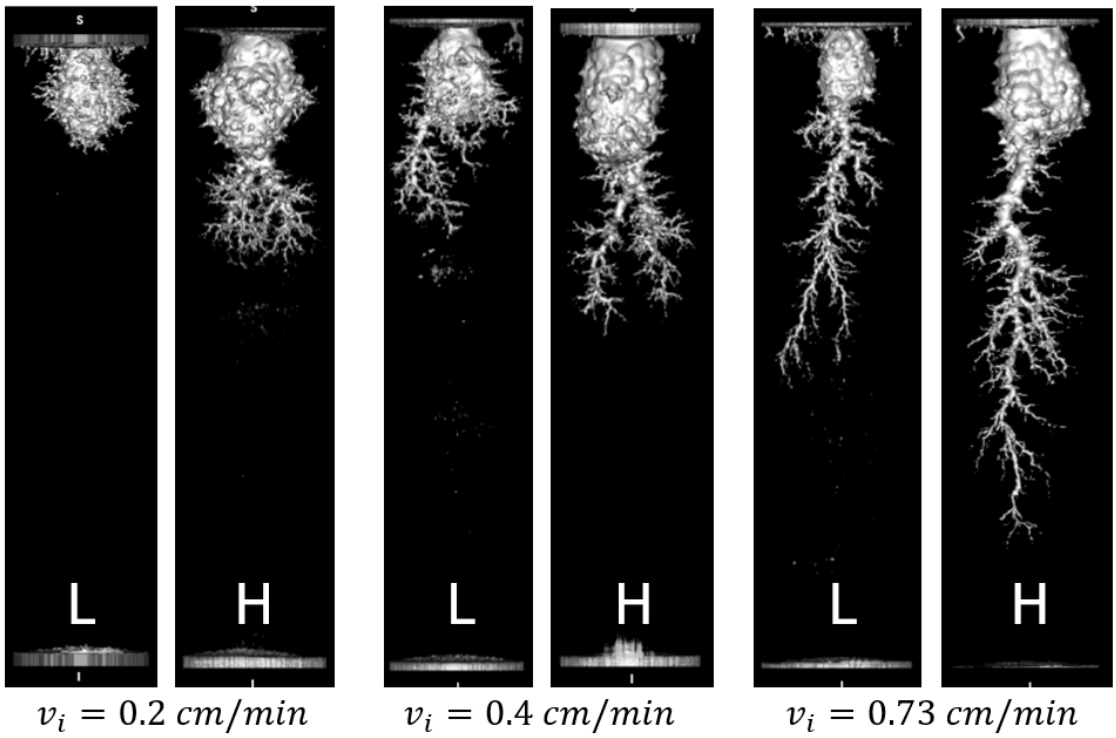

Figure 17. CT scan images of injected volume comparison tests. Interstitial velocity increasing from left to right

Figure 18 shows the cavity volume and wormhole length as a function of interstitial velocity for high-volume and low-volume experiments. Overall, the dissolution structure dimensions increased by increasing the jetting time (injected volume). The increase of cavity volume and wormhole length from the high-volume experiments to the low-volume tests is more significant as the interstitial velocity increases. Moreover, cavity volume for low-volume experiments decreases as interstitial velocity increases, while the cavity volume for the high-volume tests has an unclear trend. Meanwhile, wormhole length presents a similar increasing behavior by increasing the interstitial velocity, for both sets of experiments.

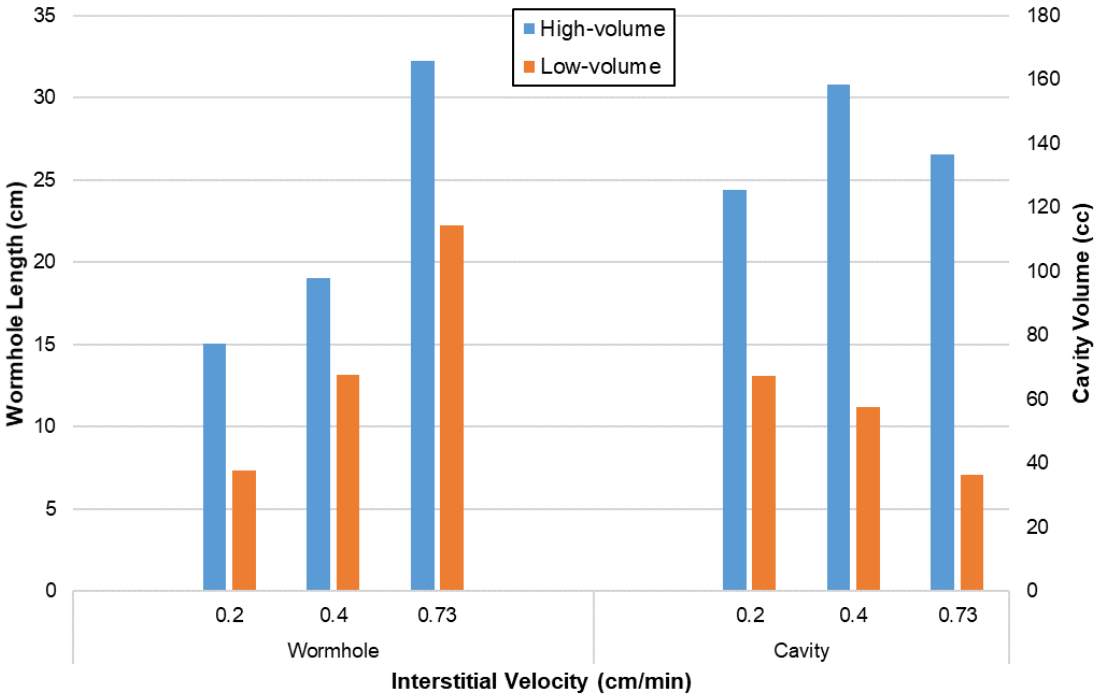

Figure 18. Cavity volume and wormhole length as a function of interstitial velocity for high-volume and low-volume experiments

Figure 19 shows the wormhole propagation rate as a function of interstitial velocity for both sets of experiments. It can be observed that at the lowest interstitial velocity, both conditions have a similar propagation rate. However, at higher interstitial velocities, the two cases differ. The high-volume tests result in lower propagation rates as most of the additional acid is spent in enlarging the cavity and wormhole structures, instead of reaching further into the sample.

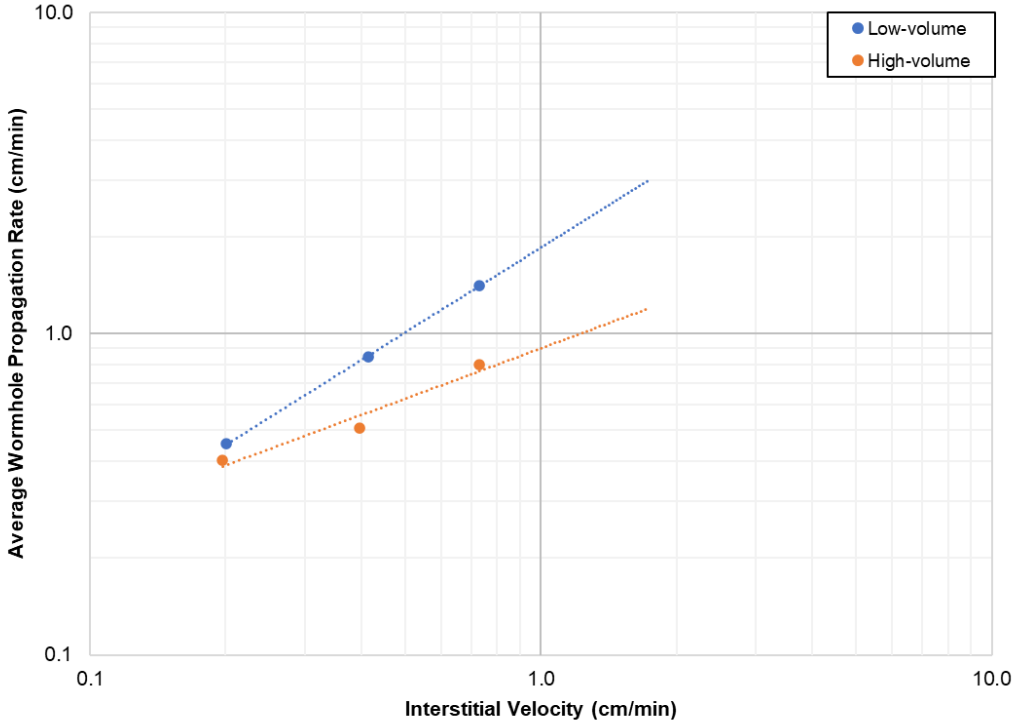

Figure 19. Wormhole propagation rate as a function of interstitial velocity for high-volume and low-volume experiments

Figure 20 shows the cavity growth rate and cavity enlargement rate as a function of interstitial velocity for both sets of experiments. Note that the cavity growth rate refers to the average depth increase of the cavity over the jetting time (cm/min), and the cavity enlargement rate refers to the average volume increase of the cavity over the jetting time (cc/min). It is observed that at lower interstitial velocities (0.2 and 0.4 cm/min), the cavity enlargement rate is relatively similar for both data sets. However, the overall behavior of the cavity enlargement rate for the low-time experiments shows a slight decrease as the interstitial velocity increases, meaning that at higher v_i values and low jetting times, less acid is spent in cavity formation, and more acid is spent in wormhole propagation. On the contrary, for the high-time experiments, the average cavity enlargement rate is almost

constant for all v_i conditions, implying that most of the additional acid is spent in cavity formation, which causes a reduction in the average wormhole propagation rate, as observed in Figure 20. In addition, Figure 18 also shows a higher cavity growth rate for the low-time tests, compared to the high-time experiments. This behavior is attributed to the similar cavity depths resulted in both data sets. These results indicate that the cavity growth rate is inversely correlated with time, meaning that as the jetting time increases, the cavity growth rate decreases. Moreover, as interstitial velocity increases, the cavity growth rate shows a slightly decreasing behavior for both data sets.

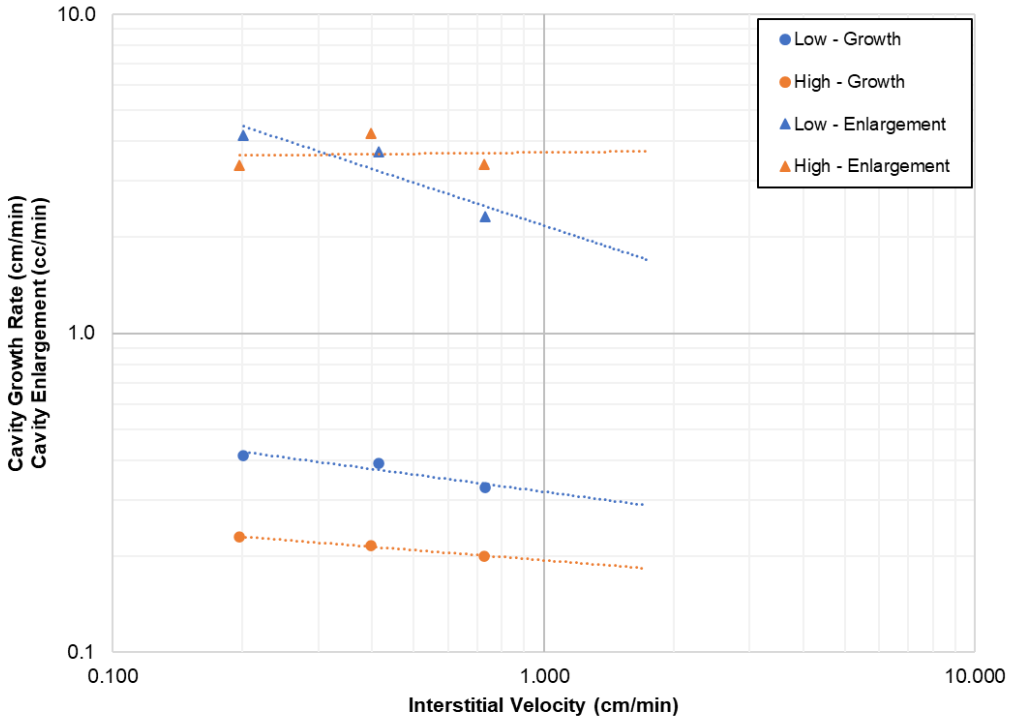

Figure 20. Cavity growth rate and cavity enlargement rate as a function of interstitial velocity for high-volume and low-volume experiments

In general, the observed behaviors on wormhole propagation and cavity formation indicate that cavity growth rate and wormhole propagation rate are reduced as the jetting

time increases, allowing cavity enlargement to dominate the dissolution process at high jetting times. Therefore, increasing the acid volume (jetting time) does not necessarily lead to better treatment efficiency since the acid volume variation has a greater impact on the cavity volume, rather than in wormhole length. This means that increasing acid volume can result in bulker cavities instead of extended reach structures.

3.2.2. Effect of Nozzle Size on Dissolution Structures

In this study, the effect of vary the nozzle size at a constant stand-off distance rock face was evaluated. Two nozzle diameters were used, 0.0225-inch and 0.019-inch, which represents a 15% decrease in nozzle diameter. Table 5 shows the experimental conditions for the samples analyzed in this section. Note that due to pressure limitations of the injection pump while using the smaller nozzle size, the jetting velocity was reduced to 65 ft/s for both data sets. The inlet temperature was maintained at 190 °F with a variation of +/- 2 °F during the test. These tests attempted to simulate a nozzle size modification of a downhole liner, where the stand-off distance in our experiments represents the distance between the liner's outer diameter and the reservoir face.

Table 5. Experimental conditions for nozzle size investigation

Experiment Number	Set	Interstitial Velocity (cm/min)	Jetting Velocity (ft/s)	Jetting Time (min)	Nozzle Size (in)	Acid System
IL15	Baseline	0.2	65	16.10	0.0225	Modified Acid
IL16		0.4		15.73		
IL11		0.71		15.81		
IL13	Decreased Nozzle Size	0.2	65	15.73	0.019	Modified Acid
IL14		0.4		15.90		
IL12		0.71		16.36		

Figure 21 presents the CT image results for the experiments using the two nozzle sizes. Note that at the lower interstitial velocities, the smaller nozzle resulted in shorter wormholes, and at the highest matrix flux, the results reversed. Additionally, cavity dimensions are almost constant for all experiments, for both nozzle sizes.

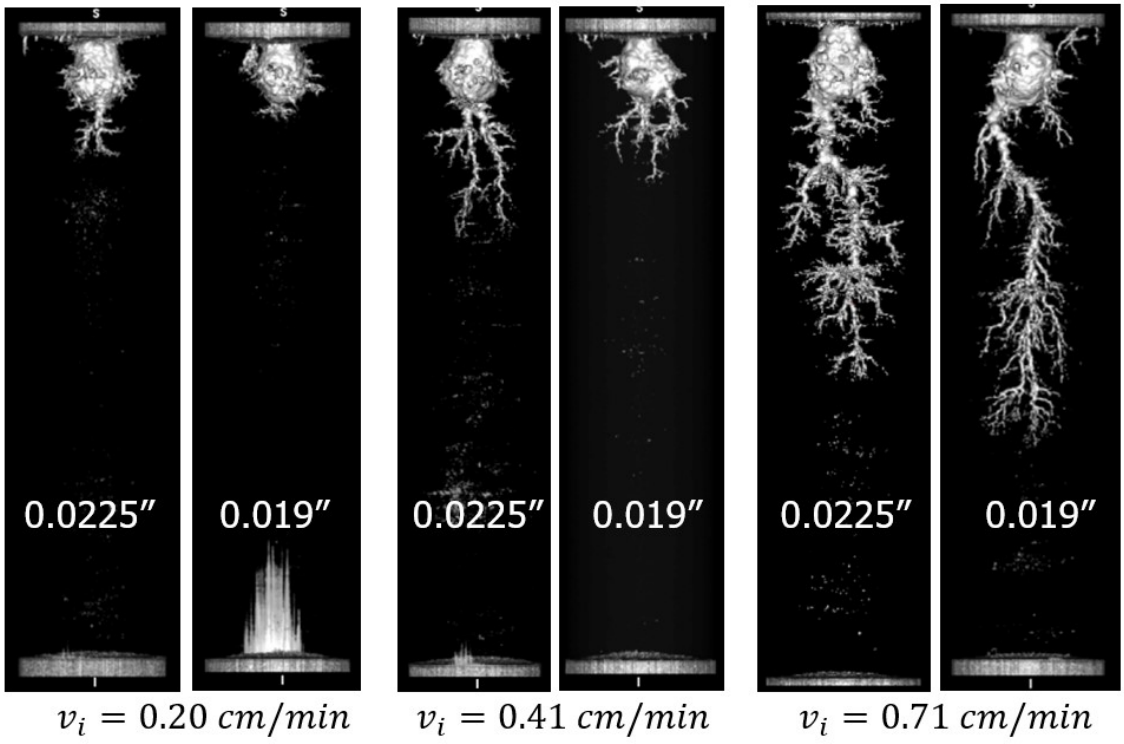

Figure 21. Effect of nozzle size on dissolution structures with interstitial velocity increasing from left to right

Figure 22 shows the wormhole length and cavity volume as a function of interstitial velocity for both nozzle sizes. It is observed that for the smaller nozzle size, the wormhole length and cavity increase as the interstitial velocity increases. Moreover, for larger nozzle size, wormhole length also increases with increasing v_i; however, the cavity volume is almost constant for all v_i conditions. Note that at lower v_i (0.2 and 0.4 cm/min), the larger nozzle resulted in slightly longer wormholes, and at the highest v_i the results reversed.

This deviation is attributed to permeability and porosity variations from sample to sample. Overall similar dissolution structures resulted from using both nozzle sizes. The acid jetting experimental results suggest that for a constant stand-off distance, the nozzle size variation has a negligible impact on the dissolution structures. However, experiments at higher interstitial velocities and larger nozzle size variations may lead to different results.

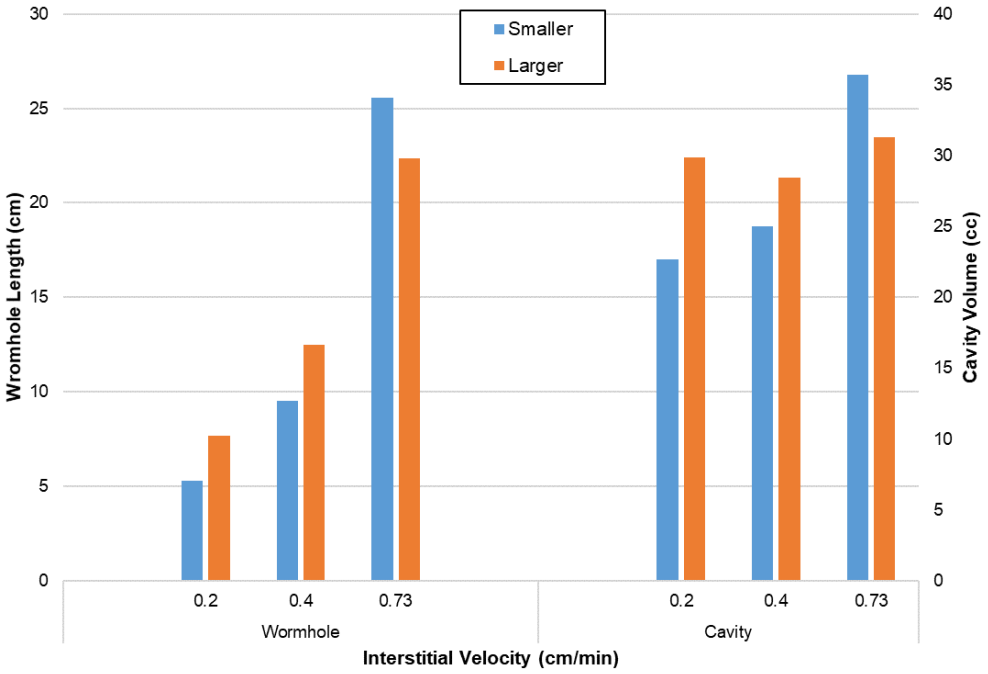

Figure 22. Wormhole length and cavity volume as a function of interstitial velocity for both nozzle sizes

3.2.3. Effect of jetting velocity on the dissolution structures

Experiments at three different jetting velocities, each at constant interstitial velocity and constant temperature, were performed to evaluate the impact of jetting velocity on wormhole propagation rate and dissolution structures. Table 6 shows the experimental conditions for all samples used in this section of the study. Note that a similar nozzle size

and acid system were used for all tests. The inlet temperature was maintained at 190 °F with a variation of +/- 2 °F during the experiments.

Table 6. Experimental conditions for jetting velocity investigation

Experiment Number	Set	Interstitial Velocity (cm/min)	Jetting Velocity (ft/s)	Jetting Time (min)	Nozzle Size (in)	Acid System
IL15	Baseline	0.2	65	16.10	0.0225	Modified Acid
IL16		0.4		15.73		
IL11		0.71		15.81		
IL5	Increased Jetting Velocity	0.2	150	16.10	0.0225	Modified Acid
IL6		0.4		15.50		
IL4		0.73		15.76		
IL19	Decreased Jetting Velocity	0.2	25	15.78	0.0225	Modified Acid
IL18		0.4		15.93		
IL17		0.71		15.81		

Figure 23 shows the dissolution structures from these experiments, where the jetting velocity increase from left to right at each interstitial velocity condition. Consistently for all evaluated interstitial velocities, larger jetting velocities resulted in increased cavity dimensions, both depth, and width. On the contrary, the wormhole structures had almost negligible variations for the same interstitial velocity and different jetting conditions. This indicates that the jetting velocity controls cavity growth and has no significant impact on wormhole propagation. This feature of the modified acid system has potential benefits in field operations since using less pumping power (lower v_{jet}) will result in wormholes propagating to similar lengths into the formation as if higher pumping power were used.

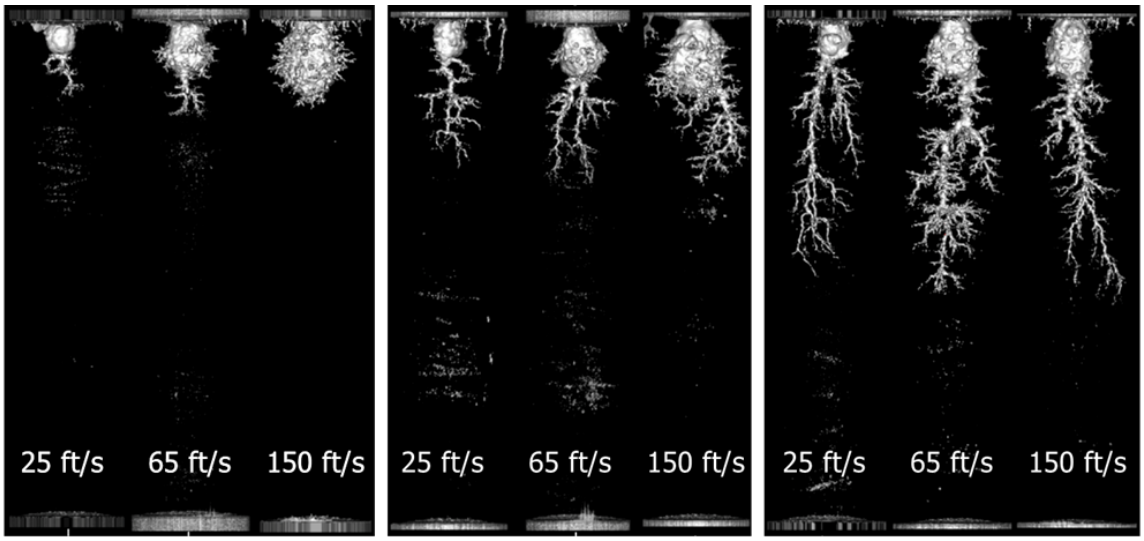

Figure 23. Effect of jetting velocity on dissolution structures with interstitial velocity and jetting velocity increasing from left to right

Figure 24 presents the cavity growth rate and cavity volume as a function of interstitial velocity for all jetting velocity conditions. Overall, at the same interstitial velocity condition, the cavity growth rate and volume increase by increasing the jetting velocity, resulting in larger and bulkier cavities as jetting velocity raises. It is also observed that at a jetting velocity of 150 ft/s, the cavity volume and cavity growth rates decrease as interstitial velocity increases. However, this behavior varies at lower jetting velocity conditions. For jetting velocities of 25 ft/s and 65 ft/s, the cavity volume shows no significant variation as interstitial velocity increases. In addition, cavity growth rate presents a different behavior for each jetting velocity condition as v_i increases. At 150 ft/s, the cavity growth rate decreases as v_i increases, while at 65 ft/s, the cavity growth rate increases as v_i increases. Lastly, at 25 ft/s, low v_i shows a reduced cavity growth rate while at higher v_i values, there is not much variation on the cavity growth rate. These

results suggest that at intermediate to high jetting velocity, cavity formation strongly depends on jetting velocity as well as interstitial velocity. On the contrary, at low jetting velocities, the impact of interstitial velocity on cavity formation is almost negligible.

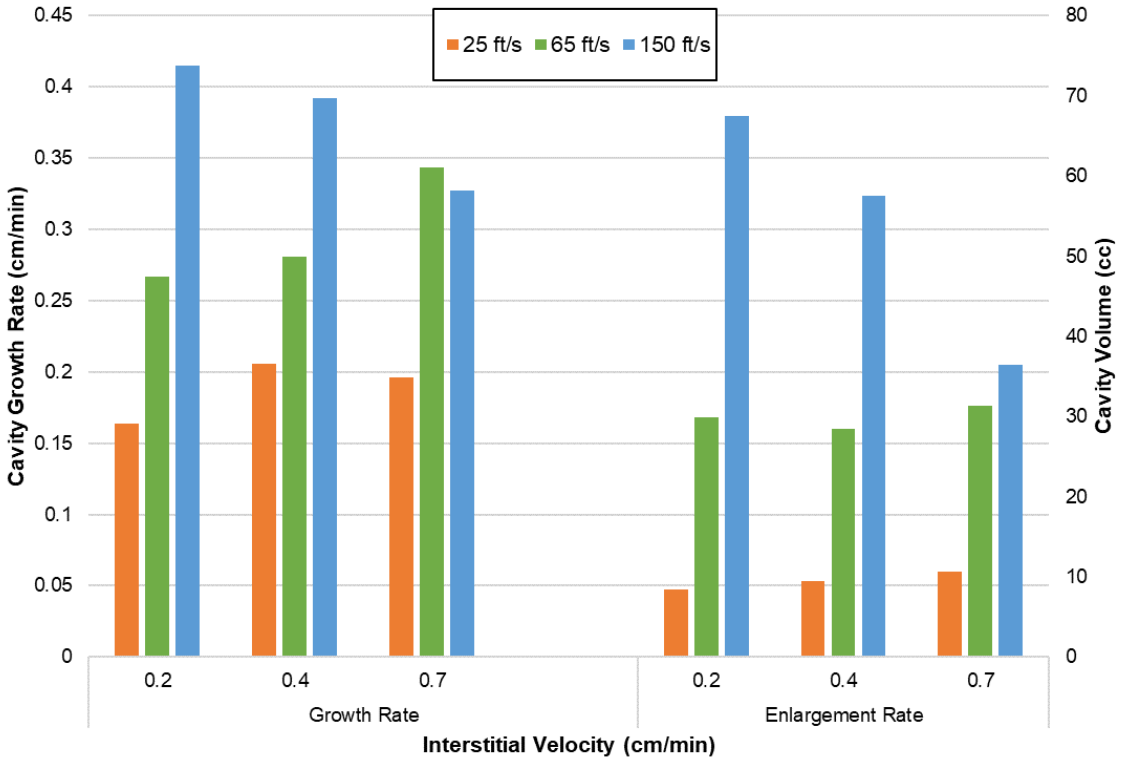

Figure 24. Cavity growth rate and cavity volume as a function of interstitial velocity for all jetting velocity conditions

Figure 25 shows the average wormhole propagation rate as a function of interstitial velocity, where each data set represents a constant jetting velocity. The v_{jet} values were 25 ft/s, 65 ft/s, and 150 ft/s. It is observed that for the modified acid system, the wormhole propagation rate has minor variation as the jetting velocity increases. However, the lowest jetting velocity of 25 ft/s had a slightly lower wormhole propagation rates at all v_i conditions. Additionally, the wormhole propagation rate rises significantly by increasing

the interstitial velocity, similarly to the findings of previous researchers in matrix acidizing and acid jetting.

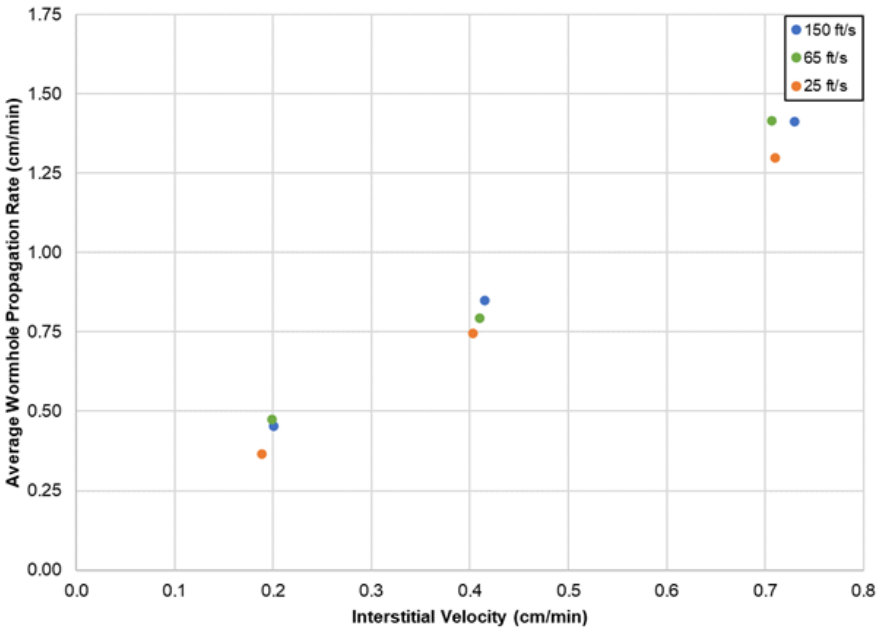

Figure 25. Wormhole propagation rate as a function of interstitial velocity for all jetting velocity conditions using a modified acid system

At low to intermediate jetting velocities (25 and 65 ft/s), the wormhole propagation rates are almost equivalent to the wormholing rates at the highest jetting velocity (150 ft/s) (Figure 23). In addition, jetting at lower to intermediate velocities result in significant reductions of cavity dimensions. These results lead to two potential benefits of using the modified acid system at lower jetting velocity. First, by decreasing the jetting velocity, the required injection rates to reach the jetting condition are lowered. Thus, surface pumping power is reduced. This, without diminishing the extension of the wormholes into the formation. The second potential benefit is that due to the lower injection rates, less volume of acid is used to propagate wormholes to a certain depth. This is valid for a fixed jetting

time (same treatment time). These potential operational benefits result in cost reductions when using the modified acid system at lower to intermediate jetting velocities.

3.3. Acid Systems Comparison

This section presents a comparison of two acid systems under acid jetting experiments. Table 7 presents the experimental conditions of all the tests used in this section, for both, the modified acid and 15% HCl. Note that experiments with 15% HCl at 150 ft/s were taken from Ridner et al. (2020), the remaining experiments used in this comparison were done in this study.

Table 7. Experimental conditions for acid systems comparison

Experiment Number	Set	Interstitial Velocity (cm/min)	Jetting Velocity (ft/s)	Jetting Time (min)	Nozzle Size (in)	Acid System
IL15	Baseline	0.2	65	16.10	0.0225	Modified Acid
IL16		0.4		15.73		
IL11		0.71		15.81		
IL19	Decreased Jetting Velocity	0.2	25	15.78	0.0225	Modified Acid
IL18		0.4		15.93		
IL17		0.71		15.81		
IL5	Increased Jetting Velocity	0.2	150	16.10	0.0225	Modified Acid
IL6		0.4		15.50		
IL4		0.73		15.76		
IL20	Baseline HCl	0.2	65	15.85	0.0225	15% HCl
IL21		0.4		15.85		
IL22		0.7		15.71		
IL23	Decreased Jetting Velocity HCl	0.2	25	15.95	0.0225	15% HCl
IL24		0.4		15.74		
IL25		0.7		16.33		
IB15*	Increased Jetting Velocity HCl	0.2	150	16.10	0.0225	15% HCl
IB13*		0.4		15.00		
IB14*		0.74		15.30		

* High-temperature experiments presented by Ridner et al. (2020).

Figure 26 shows the comparison of the dissolution structures resulted from acid jetting experiments with a modified acid and 15% HCl. Each pair of images shows the modified acid test on the left and the HCl test on the right, for one interstitial velocity condition. Figure 26 (a), (b) and (c) present the jetting velocities evaluated in this study, where (a) shows the baseline at 65 ft/s, (b) shows the high condition of 150 ft/s, and (c) shows the low condition of 25 ft/s. Overall, the dissolution structures from the modified acid system are more advantageous since reduced cavity dimensions were achieved, and more extended wormholes were propagated. Note that for HCl at 150 ft/s and 0.2 cm/min, the wormhole length is assumed to be equal to the cavity depth, but no wormhole is observed.

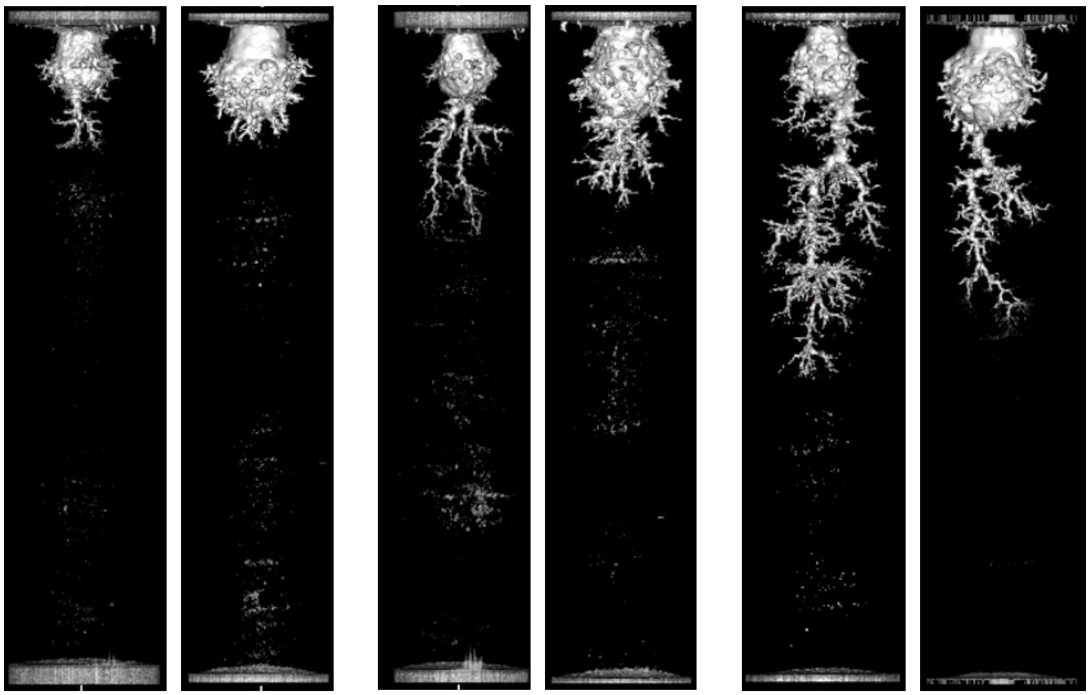

$v_i = 0.20\ cm/min$ $v_i = 0.40\ cm/min$ $v_i = 0.70\ cm/min$

(a) $v_{jet} = 65\ ft/s$

Figure 26. Dissolution structures of experiments at various interstitial velocities, (a) 65 ft/s, (b) 150 ft/s, and (c) 25 ft/s, all at a temperature of 190 °F, using 15% HCl

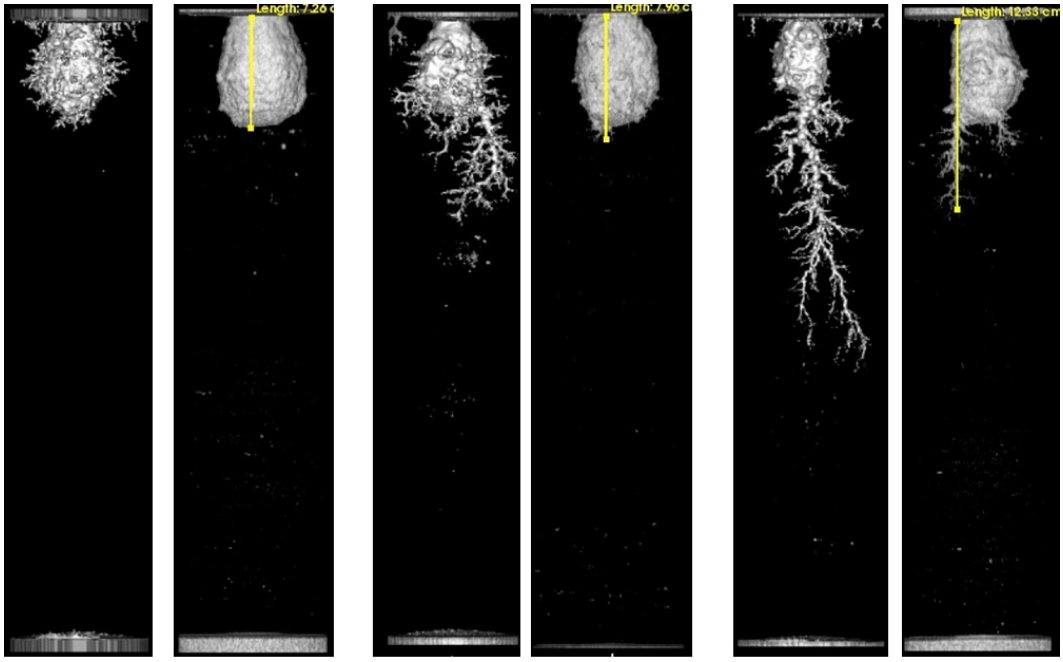

$v_i = 0.20\ cm/min$ $v_i = 0.40\ cm/min$ $v_i = 0.70\ cm/min$

(b) $v_{jet} = 150\ ft/s$

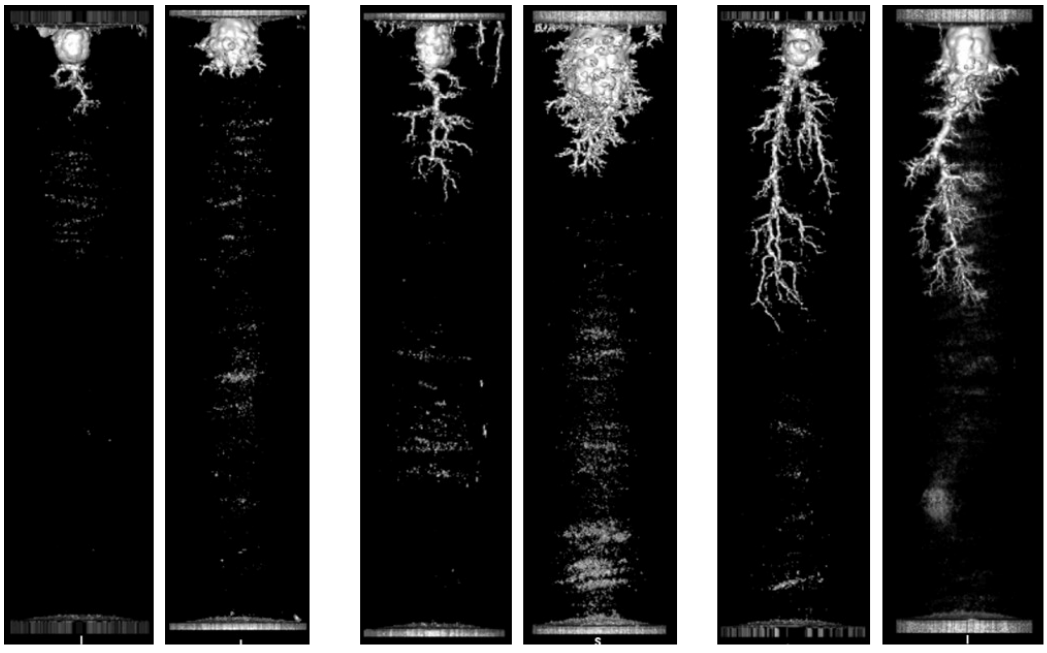

$v_i = 0.20\ cm/min$ $v_i = 0.40\ cm/min$ $v_i = 0.70\ cm/min$

(c) $v_{jet} = 25\ ft/s$

Figure 26 Continued.

Figure 27 presents the wormhole propagation rate as a function of interstitial velocity for the modified acid system and 15% HCl. In general, for both acid systems, at the same jetting velocity, the wormhole propagation rate increases as the interstitial velocity increases. Note that for the same interstitial velocity, the wormhole propagation rate of the modified acid system is almost constant for all the jetting velocity conditions. However, HCl presents more variability on the wormhole propagation rate at different jetting conditions. In addition, HCl tests at 0.7 cm/min show decreasing wormhole propagation rate as jetting velocity increases. Overall, at the lowest interstitial velocity, the modified acid system matched the HCl results and over-performs HCl as interstitial velocity increases. Operationally, these results suggest that, compared to HCl, less volume of the modified acid system is required to propagate a wormhole a specific length.

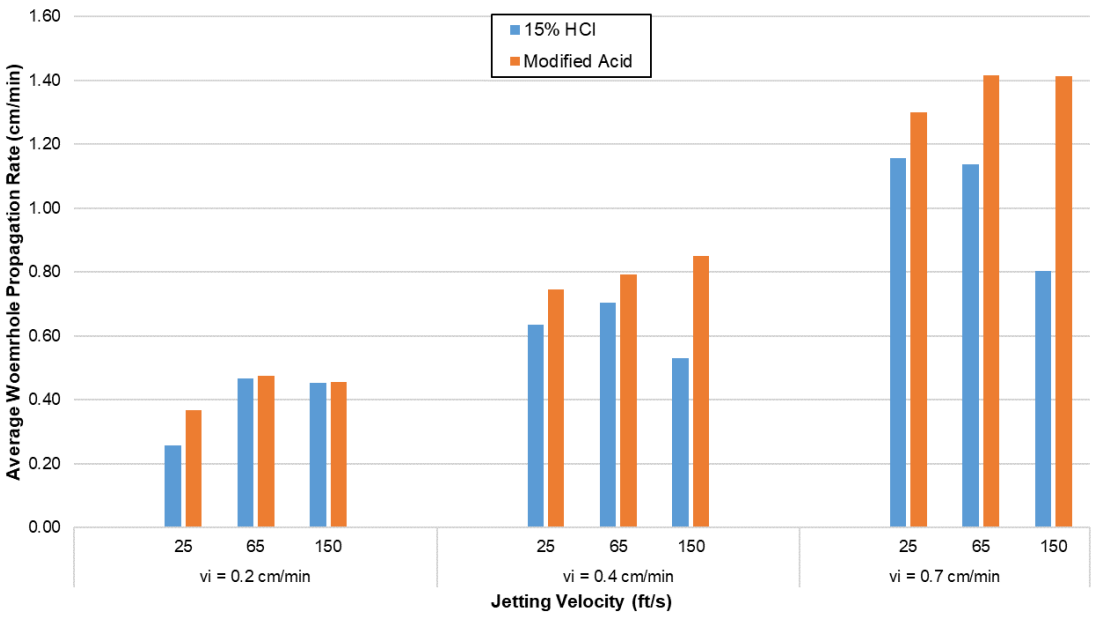

Figure 27. Comparison of wormhole propagation rate as a function of interstitial velocity for all jetting velocity conditions using 15% HCl

Figure 28 presents the cavity volume rate as a function of interstitial velocity for all jetting conditions, using a modified acid system and HCl. Note that for both acid systems at the same v_i condition, cavity volume increases as the jetting velocity increases. Moreover, both acid systems at 150 ft/s present a reduction in cavity volume as the interstitial velocity increases. Note that HCl shows higher variability in the resulted cavity volume as interstitial velocity varies. On the contrary, HCR presents almost constant cavity volume at 65 and 25 ft/s, and decreasing behavior at 150 ft/s, while interstitial velocity increases. Overall, the modified acid system generates smaller cavity volumes than 15% HCl. The difference in cavity volume is more pronounced as jetting and interstitial velocity increase.

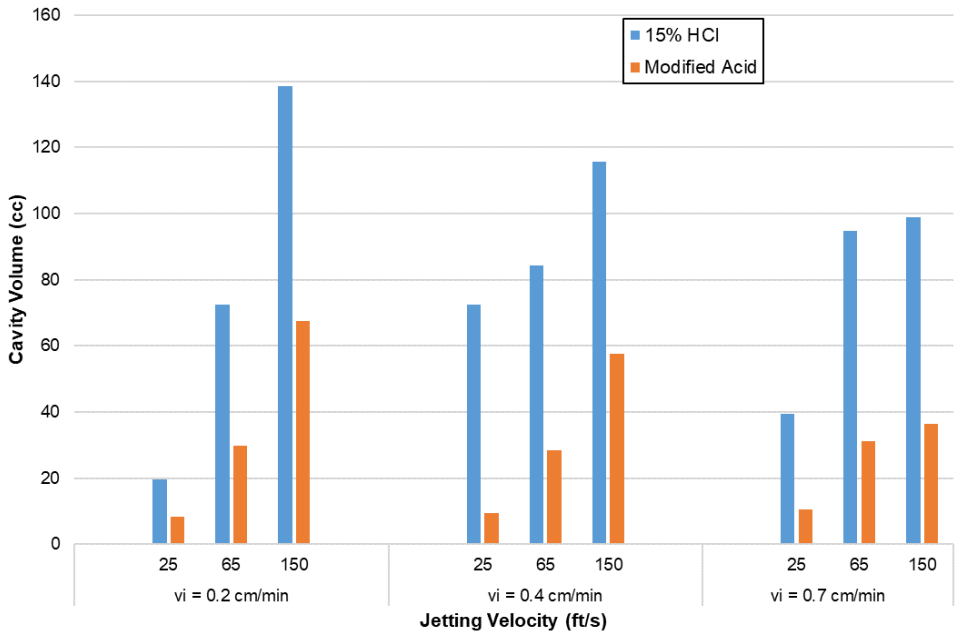

Figure 28. Comparison of cavity volume as a function of jetting velocity and interstitial velocity for the modified acid and HCl

Results from Figure 28 indicate that when jetting under similar conditions, the modified acid system has more control over cavity formation than 15% HCl, allowing more acid to be spent in wormholing instead of cavity formation. In addition to cavity volume, the cavity growth rate was also evaluated for the modified acid and HCl. Figure 29 presents the cavity growth rate as a function of interstitial velocity for all jetting conditions and both acid systems. Note that for all evaluated conditions, the modified acid system over-performed HCl and resulted in reduced cavity growth rates.

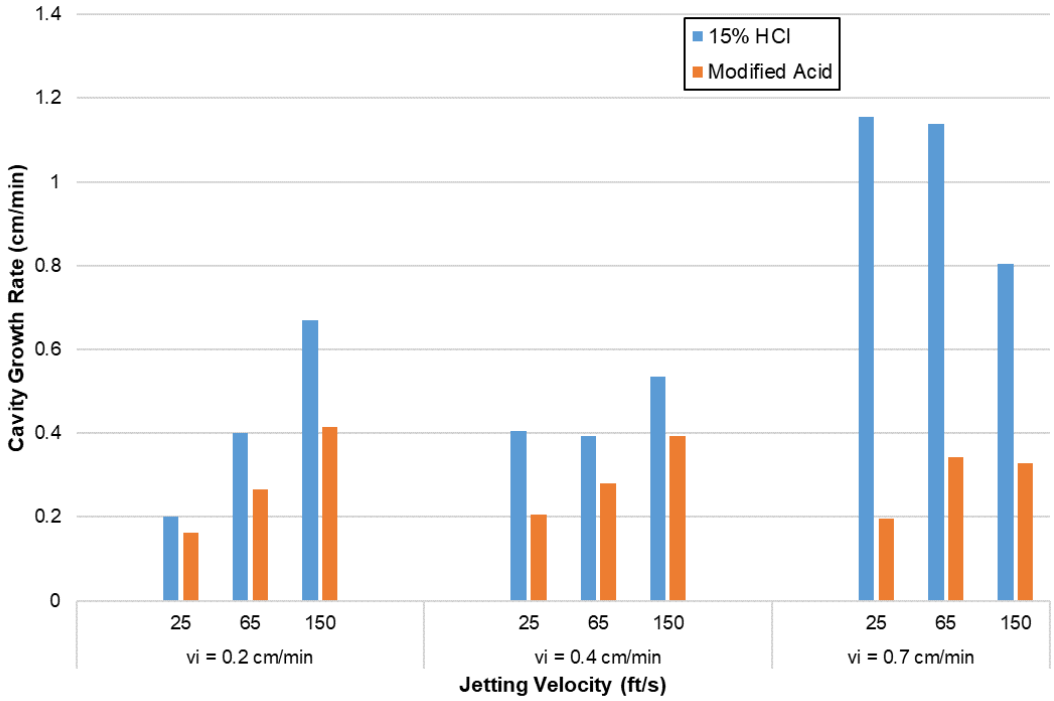

Figure 29. Comparison of cavity growth rate as a function of jetting velocity and interstitial velocity for the modified acid and HCl

The results presented in this section indicate that under acid jetting conditions, the dissolution structures resulted from using the modified acid system are preferred over results from 15% HCl. The controlled reaction rate of the modified acid system with

carbonate rocks allows improved cavity control and utilizes the acid more efficiently to propagate more extended wormholes into the rock. The enhanced wormholing rates are more evident as interstitial velocity increases, while cavity control is evident at all jetting and interstitial velocity conditions.

3.4. Lessons Learned

In this study, the investigated variables were jetting velocity, nozzle size, jetting time, and acid system. All variables were studied at a temperature of 190 °F. Individual data sets were used to investigate each variable, in which only the variable in question was modified from sample to sample. However, samples IL1, IL7, IL8, and IL9 did not meet this criterion. The details and lessons learned during these experiments are presented below.

3.4.1. Sample IL1

For this test, the experimental condition out of the desired range was temperature. The average inlet temperature was 110 °F, which is 80 °F below the desire experimental temperature (190 °F). It was found that the thermal insulation system allowed excessive heat losses from the flow line connecting the water bath and the core holder. The solution was to acquire a heating tape to increase the temperature of the tubing section to 190 °F. This additional heating system was not designed to increase the fluid temperature since the residence time in the line was negligible for this purpose. This system was designed to reduce the heating losses along the line by reducing the temperature difference of the injected fluid and the tubing, which allowed the injected fluid to reach the core at the

desired experimental temperature. It is recommended to tight the heating tape firmly to the flow lines before each test. This maximizes the contact area of the heating tape and the flow line and minimizes the heat losses.

3.4.2. Sample IL7 and Sample IL8

These experiments were intended to evaluate the effect of increasing the jetting time from 15 min to 45 min, using the modified acid system. The experimental conditions for both tests were jetting velocity of 150 ft/s, interstitial velocity of 0.2 cm/min, and temperature of 190 °F. Figure 30 shows samples IL7 and IL8 after the acid jetting tests. Note that due to the prolonged jetting time and the low matrix flux, the cavities width reached the edge of the core, causing a "side breakthrough." In practice, the "side breakthrough" is represented by an abrupt pressure increase in the LabVIEW program and upstream pressure gauge. At this point, it is recommended to stop the experiment to prevent further damage to the experimental apparatus. In addition, due to the combined effect of the "side breakthrough" and high confining pressure onto the core, sample IL8 was broken into two sections (circled in red in Figure 30). This caused the rubber sleeve inside the core holder to fail. Experimentally, the sleeve failure is identified by pressure equilibrium between the confining pressure and the upstream pressure. In order to prevent similar results in future tests, the maximum allowed jetting time was maintained below 40 minutes.

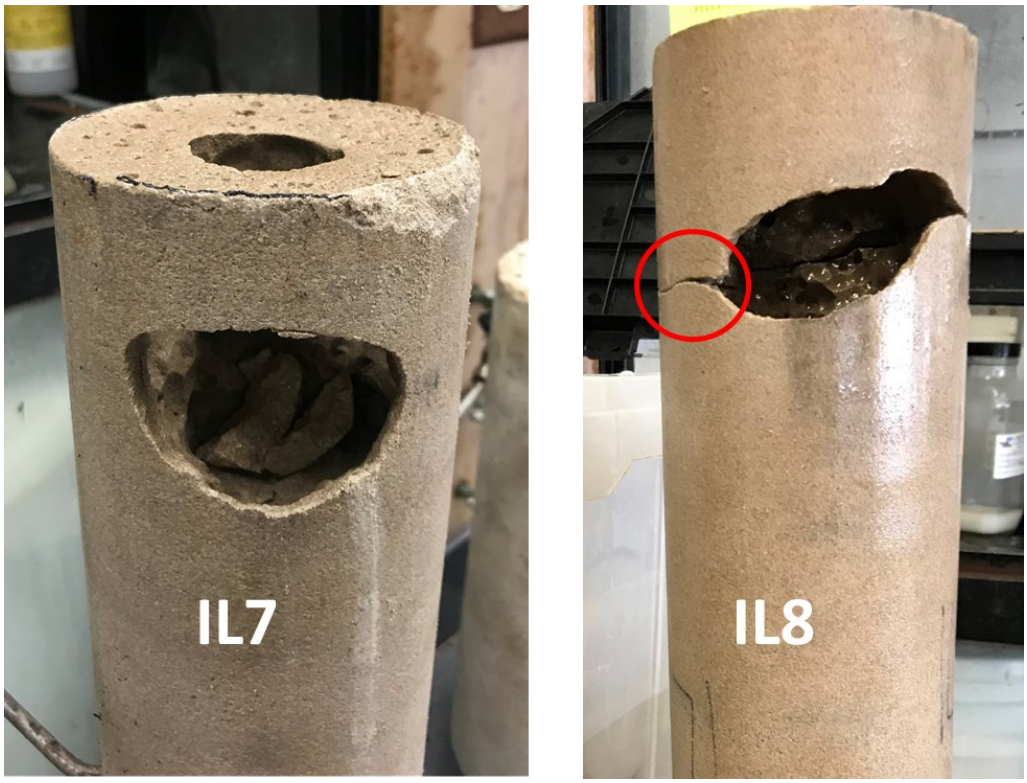

Figure 30. Samples IL7 and IL8 - Side rupture

3.4.3. Sample IL9

This experiment was considered unsuccessful due to temperature fluctuations during the jetting portion of the test. Figure 31 (a) shows the temperature profile of sample IL9, in which temperature fluctuated from 182 to 195 °F. This extreme temperature fluctuations alter the reaction rate of the acid with CaCO3, generating incomparable dissolution structures. It was found that during experiment IL9, one of the heaters inside the water bath failed, causing instability in the temperature profile. It is recommended to use both electrical heaters to allow better temperature control. In this study, the temperature was allowed to vary +/- 2 °F from the desired temperature. Figure 31 (b) shows a typical temperature profile of a successful experiment from this study.

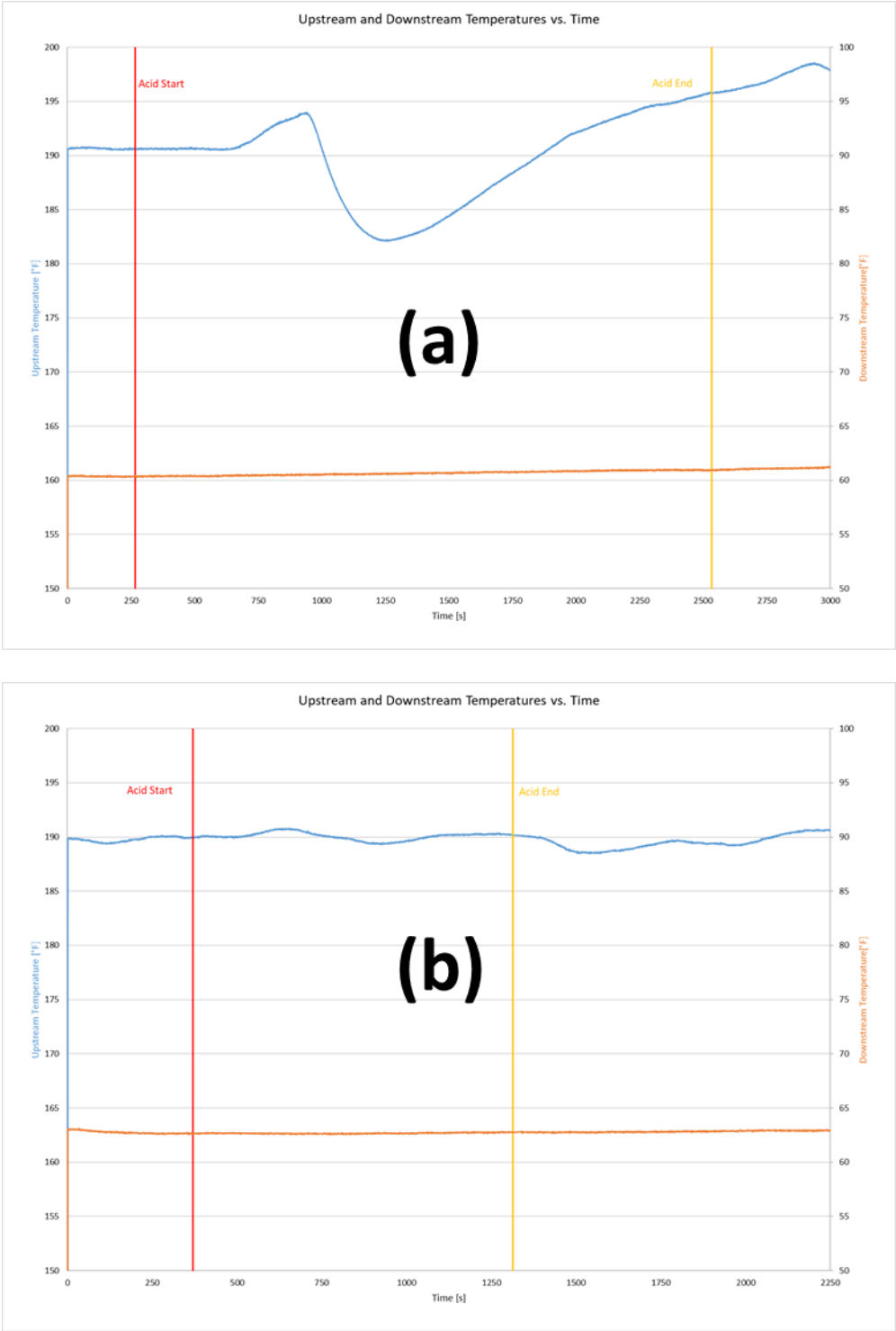

Figure 31. (a) Temperature profile of unsuccessful test. (b) Temperature profile of a typical successful test

4. CONCLUSIONS AND FUTURE WORK RECOMMENDATIONS

This study fulfilled its objectives of testing and evaluating a modified acid and conventional 15% HCl for wormholing efficiency under jetting conditions. Additionally, the effect of jetting velocity, nozzle size variation, and jetting time on the dissolution structures was evaluated for the modified acid system.

Jetting results using the modified acid system show that the jetting effect controls cavity growth and enlargement, and interstitial velocity controls wormhole propagation. However, at the jetting condition of 150 ft/s, cavity growth and enlargement were reduced as the interstitial velocity increased. Thus, the impact of interstitial velocity on the dissolution structures is greater than the jetting velocity, since depending on the conditions, interstitial velocity can control both cavity formation and wormhole propagation.

Cavity growth was found to be inversely correlated with time, where the cavity growth rate decreases as jetting time increases. However, as jetting time increases, cavity enlargement is constant and dominates the dissolution process, resulting in a reduction of the average wormhole propagation rate. Therefore, acid jetting design needs to balance cavity volume and wormhole propagation to enhance wormholing efficiency, where there preferred dissolution structures allow reduced cavity dimensions and extended wormholes.

Initial observations on the effect of nozzle size variation on the dissolution structure suggest that reducing the nozzle size at a constant stand-off distance has minor

to negligible impact on the dissolution structures. However, increasing the nozzle size difference may lead to different results.

The jetting results using the modified acid system showed promising results compared to conventional 15% HCl. Overall, the modified acid generates similar wormhole lengths as HCl at low interstitial velocity and over-performs HCl as interstitial increases. In addition, reduced cavity dimensions were observed for the modified acid systems tests for all testing conditions. These results were obtained using the same volume of each acid system. In conclusion, improved cavity control and enhanced wormholing are the main features of the modified acid system compared to conventional 15% HCl.

Future work is recommended to include non-jetting experiments at similar testing conditions and sample dimensions. These tests are recommended considering the almost negligible impact of jetting velocity on wormhole length when testing the modified acid system. Additionally, conducting large-scale experiments using the modified acid system under jetting and non-jetting conditions are recommended to calibrate the smaller-scale laboratory tests to a radial geometry, and therefore, to field scale.

REFERENCES

Abbasy, I., Ritchie, B., Pitts, M. J. et al. 2010. Challenges in Completing Long Horizontal Wells Selectively. SPE-116541-PA. *SPE Drill & Compl* **25** (02): 199 - 209.

Akbar et al. 2000. A Snapshot of Carbonate Reservoir Evaluation. SLB Oilfield Review Winter 2000-2001: 20 - 41.

Aslam, J. and Alsalat, T. 2000. High-Pressure Water Jetting: An Effective Method to Remove Drilling Damage. SPE-58780-MS. Presented at the SPE International Symposium on Formation Damage Control, Lafayette, Louisiana, 23-24 February.

Bazin, B. 2001. From Matrix Acidizing to Acid Fracturing: A Laboratory Evaluation of Acid/Rock Interactions. SPE-66566-PA. *SPE Prod & Fac* **16** (01): 22 - 29.

Beckham, R.E., Shuchart, C. E., and Buechler, S. R. 2015. Impact of Acid Jetting on Carbonate Stimulation. Paper IPTC 18360-MS presented at the International Petroleum Technology Conference. Doha, Qatar. 6-9 December.

Belostrino, E.P. 2016. Experimental Study of Multi-Stage Acid Jetting in Carbonate Rocks. MS Thesis. Texas A&M University. College Station, Texas.

Buijse, M.A. and Glasbergen, G. 2005. A Semiempirical Model to Calculate Wormhole Growth in Carbonate Acidizing. Paper SPE 96892 presented at the SPE Annual Technical Conference and Exhibition. Dallas, Texas. 9 October.

Burchette, Trevor P. 2012. Carbonate rocks and petroleum reservoirs: a geological perspective from the industry. Geological Society, London, Special Publications, 370, 17-37.

Dahroug, A., Brown, B. and Shaheen, M. 2001. Optimizing Acid Treatments with the Use of Jet Blasting Tool. Presented at the SPE/ICoTA Coiled Tubing Roundtable, Houston, Texas, 7-8 March. SPE-68364-MS.

Dong, K. 2010. Experimental Investigation for the Effect of Core Length on the Optimum Acid Flux in Carbonate Acidizing. MS Thesis. Texas A&M University.

Fowler, M. A., Gdanski, R. D., Campbell, P. et al. 2014. Unconventionals Meets Deepwater; Lower Completion Limited Entry Liner with Retrievable Ball Drop Diversion System applied in a Deepwater Brazil Carbonate Field. IPTC-18113-MS. Presented at the International Petroleum Technology Conference, Kuala Lumpur, Malaysia, 10-12 December.

Fredd, C. and Fogler, H. 1997. Chelating Agents as Effective Matrix Stimulation Fluids for Carbonate Formations. SPE-37212-MS. Presented at the International Symposium on Oilfield Chemistry, Houston, Texas, 18-21 February.

Fredd, C. and Fogler, H. 1999. Optimum Conditions for Wormhole Formation in Carbonate Porous Media: Influence of Transport and Reaction. SPE-56995-PA. *SPE J.* **4** (03): 196 - 205.

Frick, T.F. 2018. Evaluation of Acid Jetting in Matrix Acidizing Treatments in Carbonate Reservoirs. MS Thesis. Texas A&M University. College Station, Texas.

Furui, K., R. C. Burton, D. W. Burkhead et al. 2010. A Comprehensive Model of High-Rate Matrix Acid Stimulation for Long Horizontal Wells in Carbonate Reservoirs. Proc., SPE Annual Technical Conference and Exhibition, Florence, Italy.

Gdanski, R. D. 2005. Recent Advances in Carbonate Stimulation. IPTC-10693-MS. Presented at the International Petroleum Technology Conference, Doha, Qatar, 21-23 November.

Hansen, J. H. and Nederveen, N. 2002. Controlled Acid Jet (CAJ) Technique for Effective Single Operation Stimulation of 14,000 ft Long Reservoir Sections. Paper SPE-78318-MS presented at the European Petroleum Conference. Aberdeen, United Kingdom. 29–31 October.

Hill, John R. 2018. Indiana Limestone. Indiana Geological & Water Survey, https://igws.indiana.edu/MineralResources/Limestone.com (downloaded January 15 2020).

Hoefner, M. and Fogler, H. 1989. Fluid-Velocity and Reaction-Rate Effects During Carbonate Acidizing: Application of Network Model. SPE-15573-PA. *SPE Prod Eng* **4** (01): 56 - 62.

Holland, C.C. 2014. Experimental High Velocity Acid Jetting in Limestone Carbonates. MS Thesis. Texas A&M University. College Station, Texas.

Hosani, F. A., Amin, A., Ali, Y. et al. 2016. Robust Completion and Stimulation Design Methodology to Maximize Well Performance for Long Horizontal Laterals in a Giant Off-Shore Field Development. SPE-183418-MS. Presented at the Abu Dhabi International Petroleum Exhibition & Conference, Abu Dhabi, UAE, 7-10 November.

Issa, F., Abbott, J. and Akbari, A. 2014. Production Optimization of Maximum Reservoir Contact Well by Utilizing Acid Stimulation with Limited Entry Technique. SPE-

171779-MS. Presented at the Abu Dhabi International Petroleum Exhibition and Conference, Abu Dhabi, UAE, 10-13 November.

Jorden, J. D., Keller, S. R. and Junaibi, H. S. 2010. Record-Setting Horizontal Pilot Wells Drilled and Completed to Establish Feasibility of Developing Giant Offshore Field from Artificial Islands. SPE-137554-MS. Presented at the Abu Dhabi International Petroleum Exhibition and Conference, Abu Dhabi, UAE, 1-4 November.

Lucia, F. J., Kerans, C., & Jennings, J. W. 2003. Carbonate Reservoir Characterization. *J Pet Technol* **55** (06): 70 - 72. SPE-82071-JPT.

McDuff, D., Jackson, S., Shuchart, C. et al. 2010. Understanding Wormholes in Carbonates: Unprecedented Experimental Scale and 3D Visualization. SPE-129329-JPT. *J Pet Technol* **62** (10): 78 - 81.

Mishra, V., Zhu, D., Hill, A. D. et al. 2007. An Acid Placement Model for Long Horizontal Wells in Carbonate Reservoirs. SPE-107780-MS. Presented at the European Formation Damage Conference, Scheveningen, The Netherlands, 30 May-1 June.

Ndonhong, V. 2014. Observations from Experimental Acid Jetting on Limestone Carbonates. MS Thesis. Texas A&M University. College Station, Texas.

Ndonhong, V., Belostrino, E., Zhu, D., Hill, A. D., Beckham, R. E., & Shuchart, C. E. 2018. Acid Jetting in Carbonate Rocks: An Experimental Study. Society of Petroleum Engineers. SPE-180113-PA. *SPE Prod & Oper* **33** (02): 382 - 392.

Othman, A. A., Ali, Y., Sau, R. et al. 2018. A Robust Production Engineering Strategy for Extended Reach Well for Sustained Performance. SPE-193205-MS. Presented at the Abu Dhabi International Petroleum Exhibition & Conference, Abu Dhabi, UAE, 12-15 November.

Paccaloni, G. and Tambini, M. 1993. Advances in Matrix Stimulation Technology. *J Pet Technol* **45** (03): 256 - 263. SPE-20623-PA.

Pereira, A. Z., Germino, M., Paixao, L. C. et al. 2012. Used Approaches for Carbonates Acidizing Offshore Brazil. SPE-151797-MS. Presented at the SPE International Symposium and Exhibition on Formation Damage Control, Lafayette, Louisiana, USA, 15-17 February.

Purdy, Clay., Jamieson, Alexander. And Weissenberger, Markus. 2018. Lysine: hydrochloride synthetic acid compositions as alternatives to conventional acids in the oil and gas industry, WO2018018129A1.

Rahim, Z., Al-anazi, H. A., Ahmed, M. S. et al. 2013. Improved Reservoir Management Strategy via Limited Entry Multi-Stage Completion Boosts Production from Massive Carbonate Reservoirs in Saudi Arabia. SPE-166527-MS. Presented at the SPE Annual Technical Conference and Exhibition, New Orleans, Louisiana, USA, 30 September-2 October.

Ridner, D. 2018. Effect of Transport Variables on Acid Jetting in Carbonates. MS Thesis. Texas A&M University. College Station, Texas.

Ridner, D., Frick, T., Zhu, D., Hill, A. D., Angeles, R., Vishnumolakala, N., & Shuchart, C. 2020. Influence of Transport Conditions on Optimal Injection Rate for Acid Jetting in Carbonate Reservoirs. SPE-189546-PA. *SPE Prod & Oper* **35** (01): 137 - 146.

Sau, R., Shuchart, C. E. and Grubert, M. A. 2014. Advanced Completion and Stimulation Design Model for Maximum Reservoir Contact Wells. SPE-171800-MS. Presented at the Abu Dhabi International Petroleum Exhibition and Conference, Abu Dhabi, UAE, 10-13 November.

Van Domelen, M. S., & Jennings, A. R. 1995. Alternate Acid Blends for HPHT Applications. SPE-30419-MS. Presented at the Offshore Europe, Aberdeen, United Kingdom. 5 - 8 September.

Wang, Y., Hill, A. and Schechter, R. 1993. The Optimum Injection Rate for Matrix Acidizing of Carbonate Formations. SPE-26578-MS. Presented at the SPE Annual Technical Conference and Exhibition, Houston, Texas, 3-6 October.

Williams, B., Gidley, J.L., and Schecheter, R.S. 1979. Aidizing Fundamentals, Chap. 2, 5-9. Richardson, Texas: Monograph Series, SPE.

APPENDIX A

STEP-BY-STEP 3D IMAGE PROCESSING

The software used for 3D image processing are ImageJ and Horos™. The following is the step-by-step image processing procedure:

Importing Images:

1. In your office computer, open ImageJ and go to DICOM manager using the following route: Plugging, Tudor DICOM and DICOM Manager.
2. In the DICOM Manager window, select DICOM Query, and input the given "Patient Name" and "Patient ID" that identifies the scanned core.
3. Click "Study ID", and then "Retrieve to Local".
    a. By default, the documents are saved in Home (H:)/DICOMSTORE/"Patient Name". However, this can be modified by the user.
4. Transfer core files to a storage device.
5. In the Mac computer, open Horos, and click "Import".
6. Select the desire file and click "Open".
7. In the new window, select "Copy Links" to save memory space on the computer.

3D Volume Rendering:

1. For 3D volume rendering, open the image set label as "Sft Tissue 0.5".
2. On the top tool bar, select the oval tool and manipulate it to fit the core diameter. It is recommended that the ROI is smaller than the diameter of the core, so that it only captures the porous media of the core and does not the outside of the core.

3. Click “ROI”, and then “Propagate Selected ROI”.
4. In the new window, select “the entire series” to propagate the ROI for all images. For “Copy method” select “Create Aliases (modify one will modify all”.
5. Click “ROI” and then “Save Selected ROI(s)…”.
6. Click “ROI” and select “Set Pixel Values to…”, then select “Outside ROIs” and input 5,000, and click “Ok”. This changes the values outside the ROI to a fixed value so that the 3D rendering process is done only inside the selected ROI.
7. Click “3D Viewer”, and “3D Volume rendering”.
8. On the “Level of Detail” (top tool bar), select “Fine”.
9. On the “CLUT Editor” (top tool bar), select “16-bit” and the pixels histogram will appear at the bottom of the screen.
10. Manipulate the histogram points to reveal the dissolution structure, similarly to the presented in Figure 11. Double click on each point to change the color of the pixels to the desire color, white is recommended.
11. Once the desired level of clarity is achieved, click “16-bit”, and the histogram will disappear.
12. Click the magnifying glass icon to change the zoom level. It is recommended to have a consistent zoom level for all 3D visualizations.
13. Click “File”, then “Export”, and “Export to Movie”.
14. Set “Number of frames:” to 160 (or as desired), select “360 degrees” and “Horizontal” for rotation orientation. Under quality, select “Best rendering”, and “Current” size. Then, click Ok.

15. Set “Frame rate:” to desired level. 30 fps is recommended for better visualization.
16. Under “Format:” select “H264 Movie” and choose the folder for saving the movie.

Wormhole Length and Cavity Depth Measurements:

1. Click “Measurement Tool” in the top tool bar.
2. To measure the wormhole length, click and hold to start measurement from the base of the cavity and let go at the tip of the wormhole to end the measurement. Make sure the measuring line is vertically straight for accurate measurements.
    a. If the wormhole broke through the core, the wormhole length is equal to the length of the sample. There is no need to measure the length using Horos™.
3. Click “File”, “Export”, and “Export to JPEG” to export the image of the dissolution pattern with the wormhole length measurement on it. Save the file with the corresponding core ID.
4. Repeat steps 2 and 3 for cavity depth measurement.
    a. Cavity depth can also be estimated using images numbers as follows: (image number at cavity end – image number at cavity start)*image thickness (1 mm or 0.5 mm). However, it is recommended to follow steps 2 and 3 for most accurate results.

Dissolution structure volume:

1. In the home page of Horos™, open the fourth image set of the core been analyzed.
2. Scroll through the images and record the image number at the start of the cavity. Close the image set.

3. Right click on the same image set as step 1 and select “Open Sub-Selection”. Under “From:” enter the recorded image number in step 2.
4. Select the “Oval tool” and follow steps 2 through 6 of the 3D Volume Rendering section.
5. Click “ROI” and select “Grow Region (2D/3D Segmentation)”. Under “Lower Threshold” enter “-3000”, and under “Upper Threshold” enter “100”. Enter core ID under “ROI Name”. Click within area of the dissolution structure, and then “Compute”.
    a. The threshold values may vary from sample to sample, requiring slight trial and error until the correct dissolution structure is captured in the grow region.
    b. For computing the grow region, it is recommended to click an area within the wormhole section (if any), so that the wormhole structure is captured correctly.
6. Record the output values of the dissolution structure volume. If possible, take a screenshot of the computed volume window for you record (Command+Shift+4).
7. For estimating cavity volume by itself, select the image set in step 2 and record the image number at the end of the cavity.
8. Right click on the same image set as step 1 and select “Open Sub-Selection”. Under “From:” enter the recorded image number in step 2, and under “To:” enter the image number recorded in step 7 (end of the cavity).

9. Click “ROI”, “ROI Volume”, and “Compute Volume”. By default, the grow region from the previous analysis is selected, following the same threshold conditions. This allows consistent measurements of cavity volume and the volume of all the dissolution structure.
10. Record the output values for cavity volume and save an image of the grow region window.

APPENDIX B

EXPERIMENTAL RESULTS

Table 8. Experimental results of all samples (Appendix B)

Experiment Number	Set	L_{cavity} (cm)	V_{cavity} (cc)	L_{wh} (cm)	v_{wh} (cm/min)	v_{cavity} (cm/min)	$v_{Enl.\ cavity}$ (cc/min)
IL15	Baseline	4.48	32.17	7.65	0.48	0.27	1.86
IL16		4.25	28.41	12.47	0.79	0.28	1.81
IL11		5.43	31.30	22.36	1.41	0.34	1.98
IL5	Increased Jetting Velocity	6.68	67.45	7.32	0.45	0.41	4.19
IL6		6.08	57.56	13.16	0.85	0.39	3.71
IL4		5.16	36.50	22.25	1.41	0.33	2.32
IL19	Decreased Jetting Velocity	2.58	8.47	5.79	0.37	0.16	0.54
IL18		3.28	9.50	11.86	0.74	0.21	0.60
IL17		3.10	10.62	20.54	1.30	0.20	0.67
IL13	Decreased Nozzle Size	4.08	22.66	5.27	0.34	0.26	1.44
IL14		4.66	25.02	9.50	0.60	0.29	1.57
IL12		5.34	35.69	25.54	1.56	0.33	2.18
IL10	Increased Jetting Time	8.58	125.59	15.02	0.40	0.23	3.37
IL2		8.03	158.34	19.02	0.51	0.22	4.24
IL3		8.07	136.70	32.25	0.80	0.20	3.39
IL20	Baseline HCl	6.35	72.50	7.38	0.47	0.40	4.57
IL21		6.24	84.27	11.16	0.70	0.39	5.32
IL22		6.32	94.69	17.87	1.14	0.40	6.03
IL23	Decreased Jetting Velocity HCl	3.20	19.61	4.09	0.26	0.20	1.23
IL24		6.39	72.96	9.98	0.63	0.41	4.60
IL25		5.23	39.35	18.88	1.16	0.32	2.41
IB15*	Increased Jetting Velocity HCl	7.26	138.45	7.30	0.45	0.67	19.25
IB13*		6.97	115.55	7.96	0.53	0.54	10.56
IB14*		6.81	98.98	12.30	0.80	0.34	2.39

* High-temperature experiments presented by Ridner et al. (2020).

APPENDIX C

PORE VOLUMES TO BREAKTHROUGH METHODS

Two calculation methods for PV_{bt} were compared throughout the completion of this study. Both methods start from the PV_{bt} definition for matrix acidizing.

$$PV_{bt} = \frac{V_{acid}}{V_{pore}} \tag{C-1}$$

The first method assumes that all the pumped acid flows through the rock sample; then, the volume of acid is defined as the following:

$$V_{acid} = v_i t_{jet} A\emptyset \tag{C-2}$$

Substituting C-2 into C-1 and replacing the length of the core for the length of the wormhole (breakthrough was not allowed). The PV_{bt} for method one results in the following:

$$PV_{bt} = \frac{v_i t_{jet}}{L_{wh}} \tag{C-3}$$

The assumption for the first method is true for matrix acidizing experiments. However, in acid jetting, not all the pumped acid flows through the rock sample, and the pump flow rates are greater than the matrix flux to allow the jetting velocity to reach the desire values.

The second method relies on the CT images results to estimate the volume of acid spent in rock dissolution. The relationship is presented below:

$$V_{acid} = \frac{V_{CaCO_3}}{x_{15}} = \frac{V_{CaCO_3,bulk}(1-\emptyset)}{x_{15}} \quad \text{(C-3)}$$

Where the $V_{CaCO_3,bulk}$ is the dissolved volume estimated using the software Horos, and is corrected to V_{CaCO_3} by the factor $(1-\emptyset)$. The term x_{15} refers to the dissolving power of 15% HCl (0.0829 cc $CaCO_3$/cc HCl). Substituting C-3 in C-1 results in the following Equation for method two:

$$PV_{bt} = \frac{V_{CaCO_3,bulk}(1-\emptyset)}{x_{15}V_{pore}} \quad \text{(C-4)}$$

An example of both methods to estimate PV_{bt} is presented below. Sample IL20 is used for this example. The data of this sample is: v_i of 0.21 cm/min, t_{jet} of 15.85 min, dissolved $CaCO_3$ is 60.5 cc, L_{wh} is 7.38 cm, and V_{pore} is 100.6 cc.

Method 1
$$PV_{bt} = \frac{0.21(15.85)}{7.38} = 0.45 \quad \text{(C-5)}$$

Method 2
$$PV_{bt} = \frac{60.5}{0.0829(100.6)} = 7.26 \quad \text{(C-6)}$$

From the 3D image od the dissolution structure of sample IL20 (see Appendix E), it can be observed that the wormholes did not reach deeper into the sample. Thus, the acid volume to breakthrough should be a large number. Method two has a larger PV_{bt}. However, neither method was found to fully represent the efficiency of acid jetting treatments since the cavity, and wormhole growth competition is not comprehended yet.

APPENDIX D

SUMMARY OF DISSOLUTION STRUCTURE IMAGES

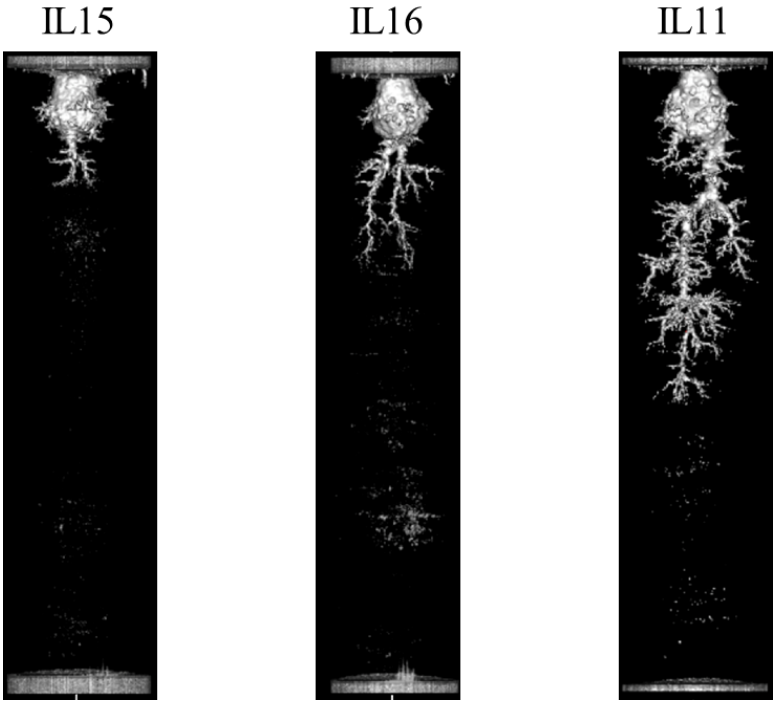

Figure 32. Dissolution structures of the baseline data set (Appendix D)

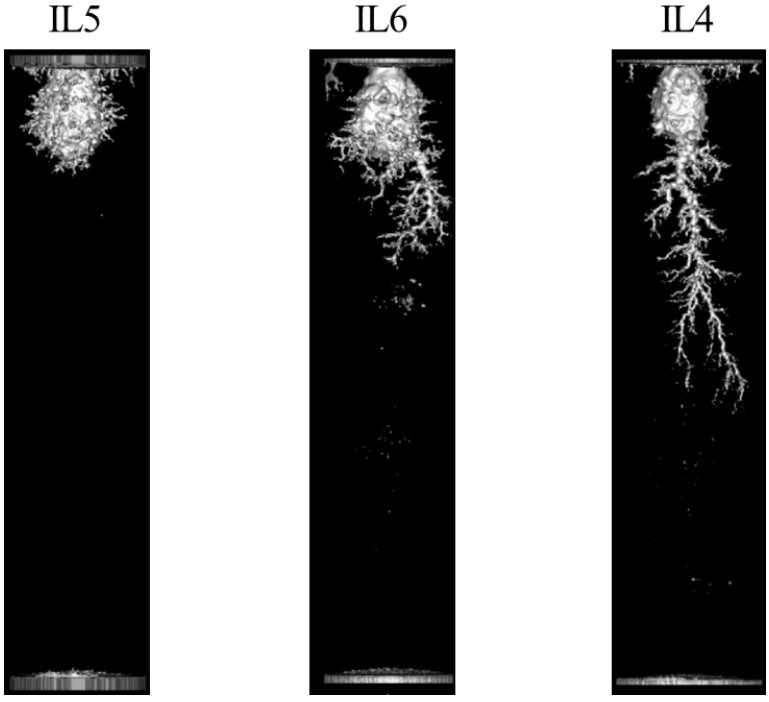

Figure 33. Dissolution structures of the increased v_{jet} data set (Appendix D)

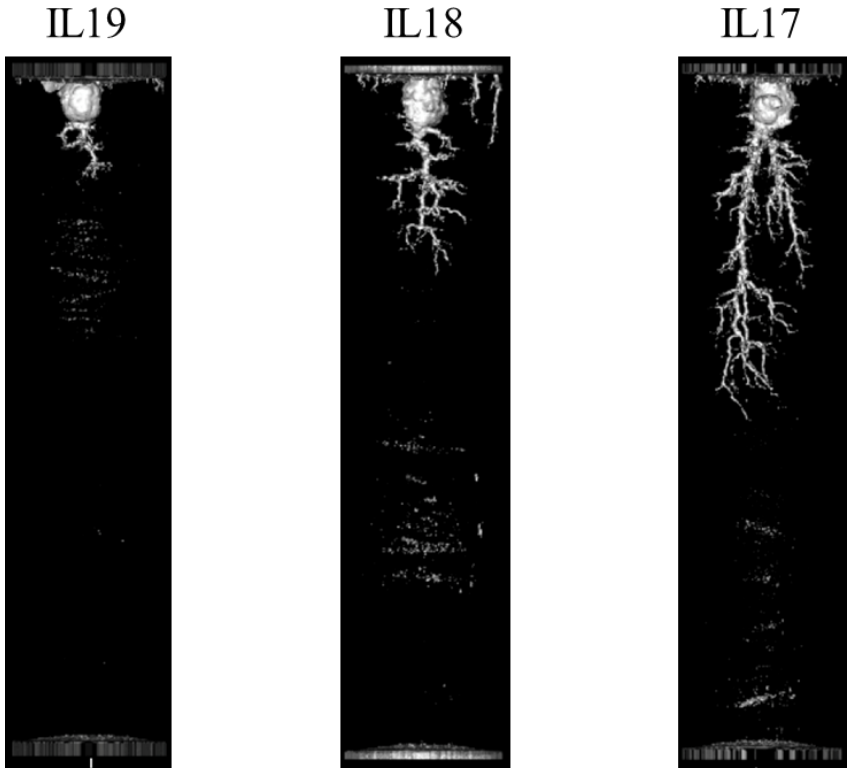

Figure 34. Dissolution structures of the decreased vjet data set (Appendix D)

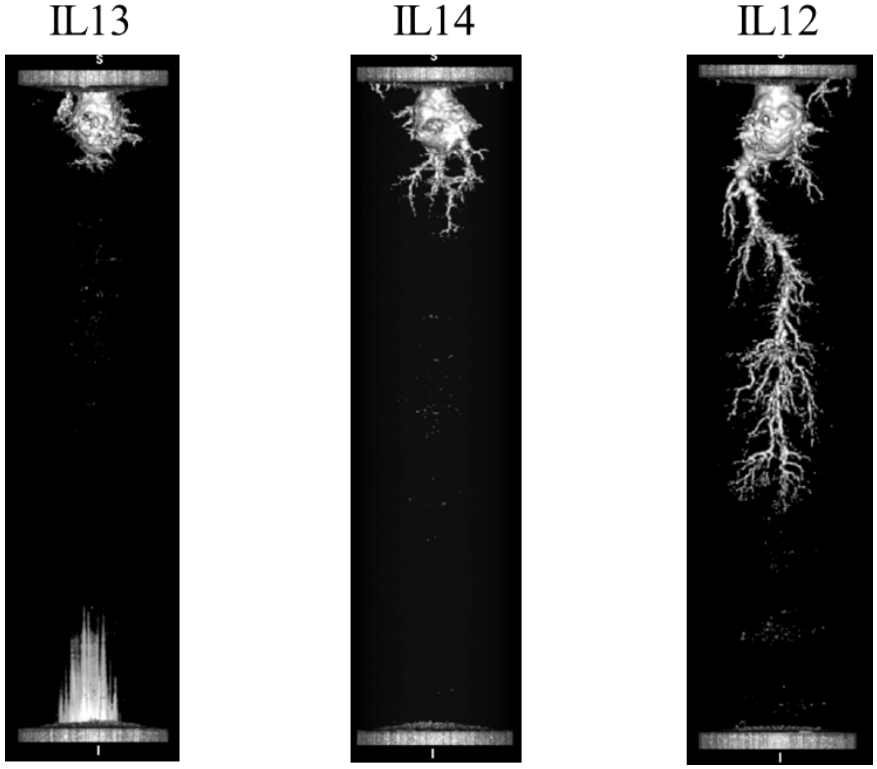

Figure 35. Dissolution structures of the decreased nozzle size data set (Appendix D)

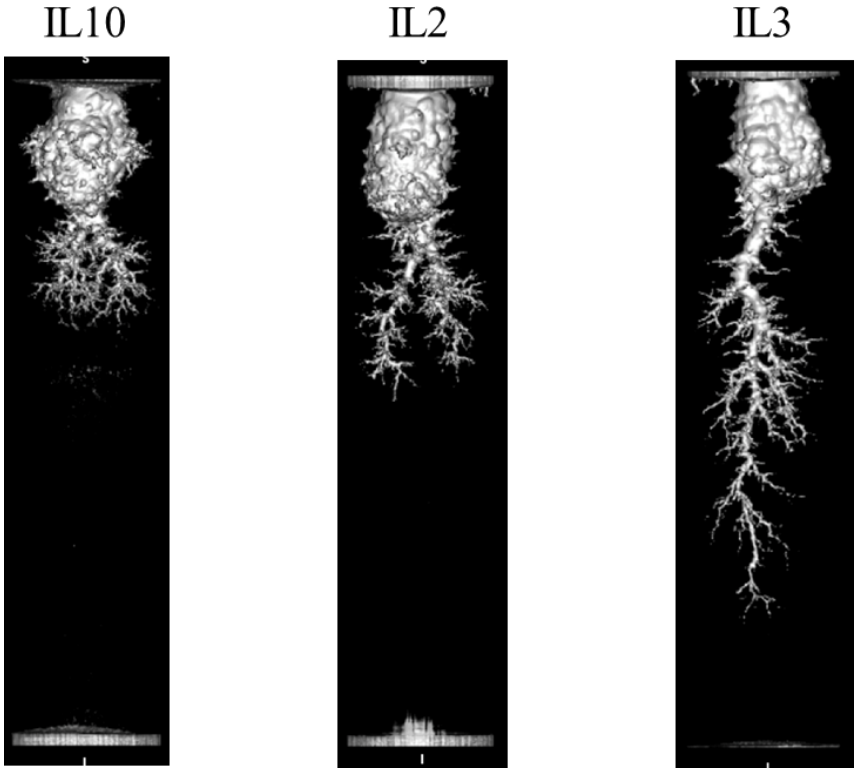

Figure 36. Dissolution structures of the increased t_{jet} data set (Appendix D)

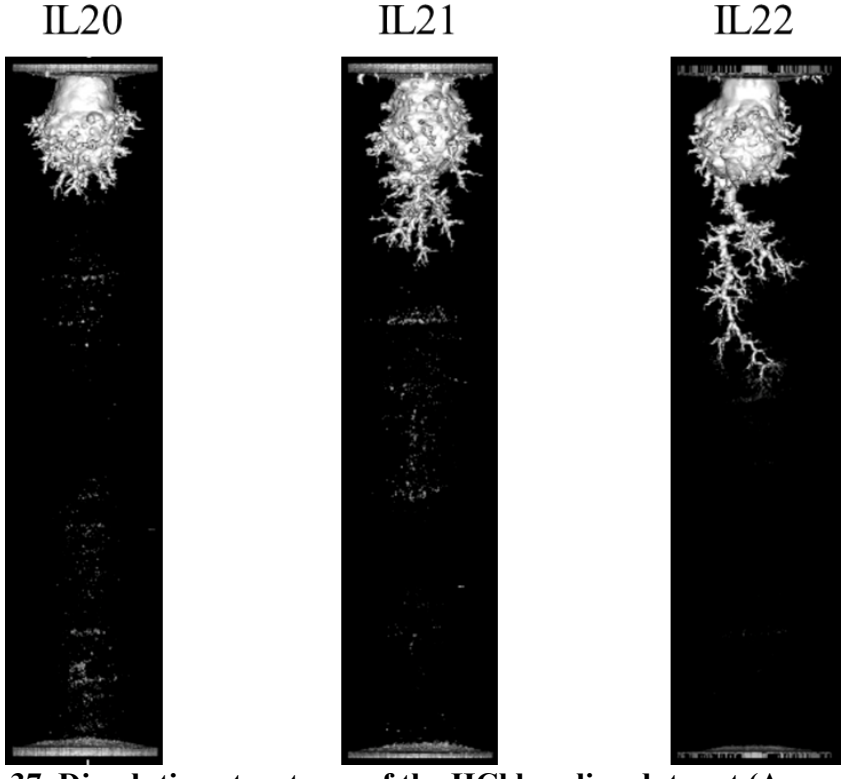

Figure 37. Dissolution structures of the HCl baseline data set (Appendix D)

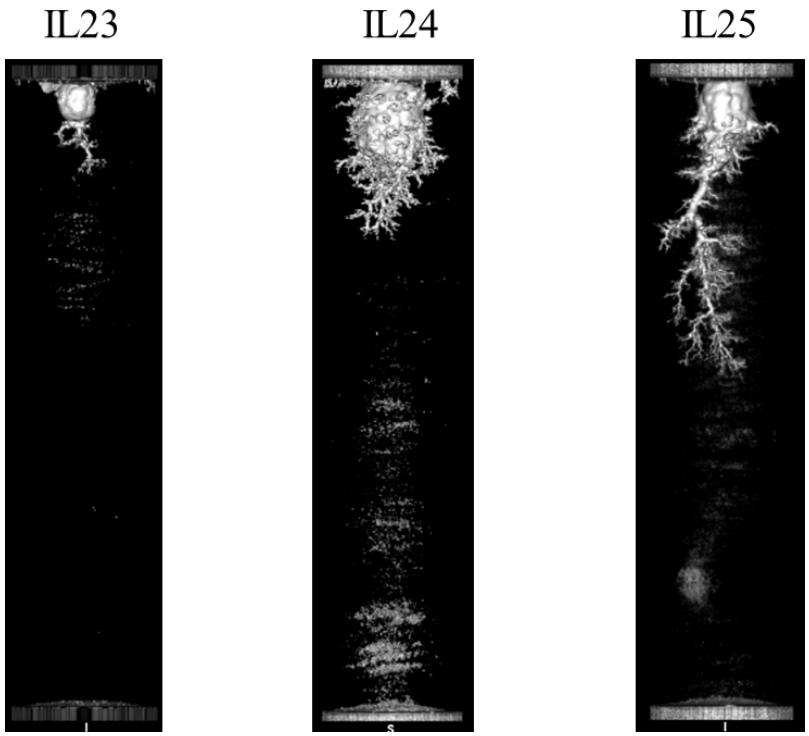

Figure 38. Dissolution structures of the HCl decreased v_{jet} data set (Appendix D)

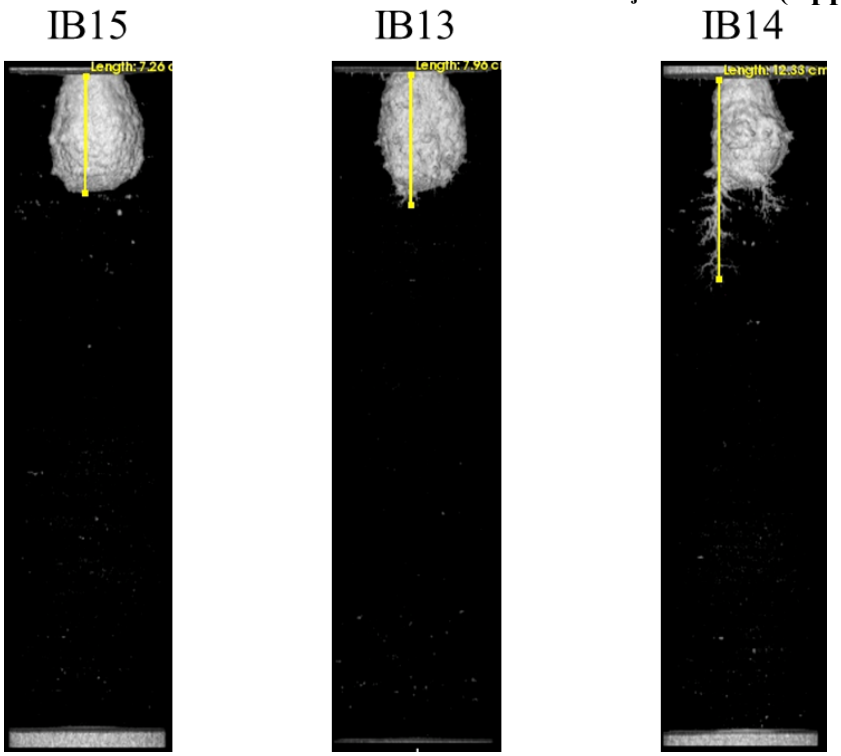

Figure 39. Dissolution structures of the HCl increased vjet data set, adapted from Ridner et al. (2020) (Appendix D)